peak RT splitting = true, intensity profiling = maximum, gap/peak ratio = 5%, refinement threshold = 80, consistency threshold = 1. The detected peaks were grouped in isotopic clusters using Chromatogram Isotopic Peak Clustering: minimum charge = 1, maximum charge = 10, maximum missing peaks = 0, first allowed gap position = 10, RT window = 0.02 min, *m/z* tolerance = 5 ppm, isotope shape tolerance = 10, minimum cluster size ration = 0.5.

Cytometric bead array

Concentration of C-X-C motif chemokine 10 (CXCL10) in CSF was determined by cytometric bead array (CBA) (BD Biosciences, San Jose, CA) according to the manufacturer's instructions.

Enzyme-linked immunosorbent assay

Concentrations of secreted protein acidic and rich in cysteine (SPARC) (R&D Systems, Minneapolis, MN) and vascular cell adhesion molecule-1 (VCAM1) (Abcam, Cambridge, MA) in 105 plasma samples were measured with commercial enzyme-linked immunosorbent assay (ELISA) kit following the manufacturer's instructions. A multivariate logistic regression was applied to construct a new diagnostic model for HAM/TSP utilizing three factors, SPARC, VCAM1, and viral load, as described previously.[11]

Result

Quantitative proteome profiling of CSFs from HAM/TSP patients

CSFs from 6 ACs and 51 HAM/TSP patients (Table 1) were processed according to the schematic workflow of this study (Fig. 1). Nonredundant 68,077 peptides from 57 individuals were detected and quantified on the Expressionist proteome server system, meanwhile 14,451

Table 1. Clinical characteristics of the CSF specimens.

Group	*N*	Age (±SD)	Gender (M/F)
AC	6	55.7 (±15.8)	4/2
HAM1_3	7	57.9 (±14.2)	3/4
HAM4_6	35	59.3 (±11.0)	11/24
HAM7_11	9	61.6 (±8.0)	1/8
Total	57	59.1 (±11.7)	19/38

CSF, cerebrospinal fluid; AC, asymptomatic carriers; HAM1_3, HAM/TSP patients whose Osame's motor disability score from 1 to 3; HAM4_6, HAM/TSP patients whose Osame's motor disability score from 4 to 6; HAM7_11, HAM/TSP patients whose Osame's motor disability score from 7 to 11.

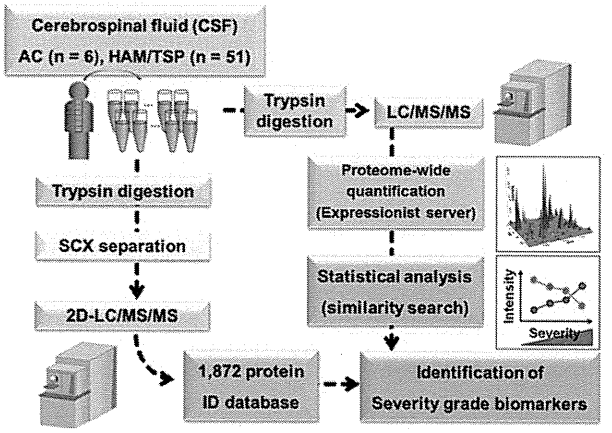

Figure 1. Schematic overview of severity grade marker screening. Cerebrospinal fluids (CSFs) from six asymptomatic carriers (ACs) and 51 HAM/TSP patients were analyzed by LC/MS/MS. Candidate peptides whose intensities had correlation with severity grades were isolated according to Pearson product-moment correlation coefficient. Candidate peptides were identified using Protein/Peptide identification database established by 2D-LC/MS/MS. HAM/TSP, human T-cell leukemia virus-1 associated myelopathy/tropic spastic paraparesis.

CSF peptides (1871 proteins) were identified by parallel 2D-LC/MS/MS analysis. To evaluate quantitative reliability of our LC/MS-based proteome profiling, observed relative concentrations of CXCL10 (Interferon gamma Inducible protein 10, CXCL10) were compared to clinical data which were measured by CBA (Fig. 2A). The result showed strong correlation (R^2 = 0.911) between two measurements, indicating that our LC/MS-based quantification results were highly credible even in the low concentration range (1–20 ng/mL).

Next, to interpret proteome-wide alterations in CSF environment of HAM/TSP patients, 1345 or 1750 proteins identified from AC or HAM/TSP patients group, respectively (Fig. 2B), were classified according to cellular component (CC, Fig. 2C and D) or biological process (BP, Fig. 2E and F) using DAVID Functional Annotation Tool. The CC analysis revealed that proteins expressed in cell projection and plasma membrane were enriched in CSF of HAM/TSP patients, in addition to specific enrichment of viral proteins. This may reflect increased invasive activity of HTLV-1-infected cells into spinal cord, which is often observed in HAM/TSP patients. Further BP analysis indicated that proteins involved in cell adhesion, cell motion, cell migration, cytoskeleton, and cell structure disassembly were highly enriched in CSF of HAM/TSP patients. These features also denoted proteome-wide environmental change in spinal cord, inducing active migration and/or invasion of lymphocytes. Proteins related to cell death and cell growth might associate with spinal inflammation in HAM/TSP patients.

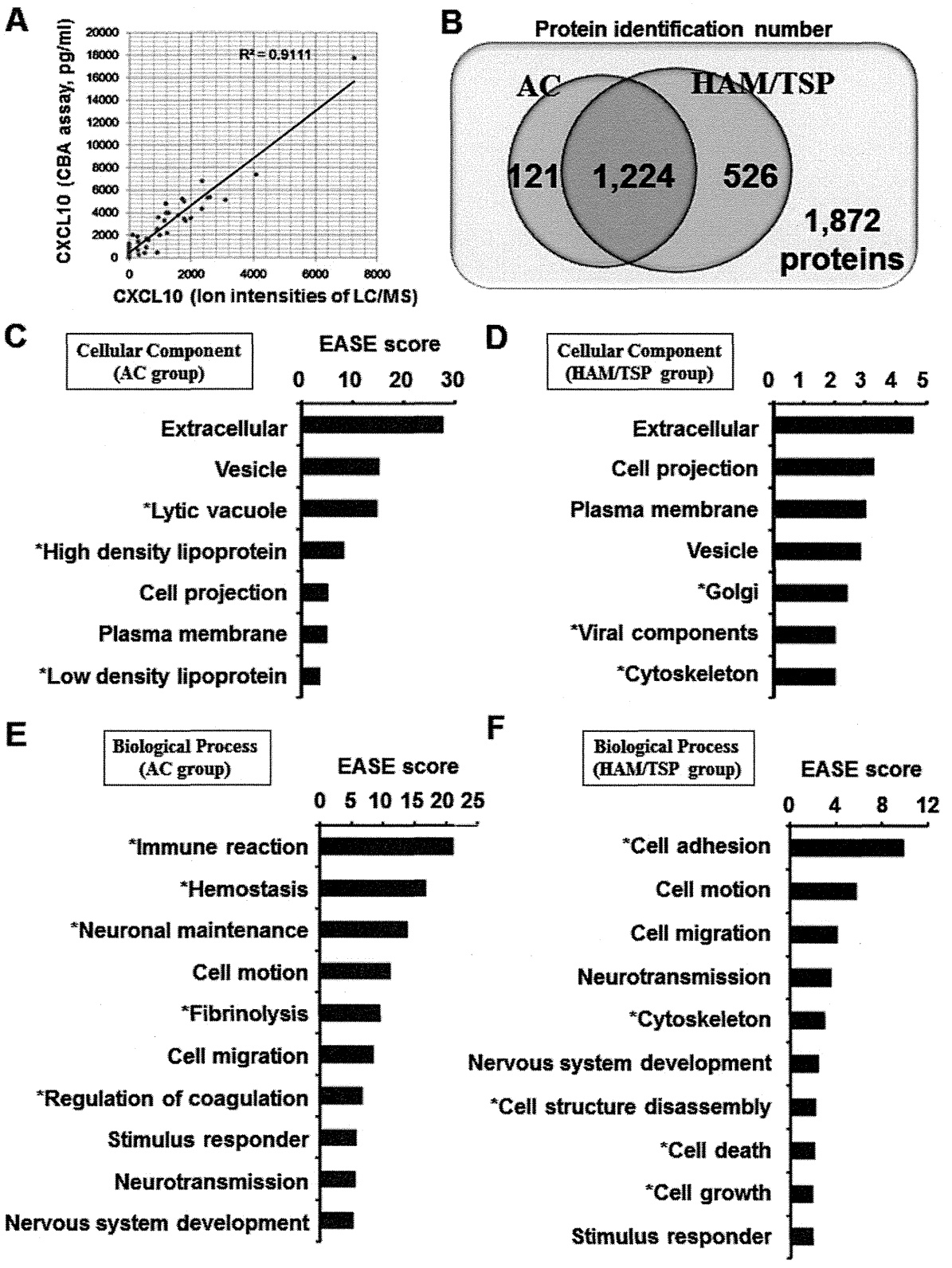

Table 2. List of 16 severity grade markers for HAM/TSP.

UniProt accession	Protein name	Amino acid numbers of identified peptide	Pearson's correlation coefficient (*R*)	*P*-value
Q9NZK5	Adenosine deaminase CECR1	247–258	0.478	5.15E-04
Q12860	Contactin-1	634–647	−0.425	9.94E-04
Q14118	Dystroglycan	222–232	−0.463	2.89E-04
Q8N2S1	Latent-transforming growth factor beta-binding protein 4	310–323	−0.463	2.90E-04
Q9Y5Y7	Lymphatic vessel endothelial hyaluronic acid receptor 1	8–18	−0.499	9.15E-05
Q16653	Myelin-oligodendrocyte glycoprotein	14–25	−0.444	5.40E-04
Q9UJJ9	N-acetylglucosamine-1-phosphotransferase subunit gamma	47–56	−0.442	5.72E-04
P13591	Neural cell adhesion molecule 1	586–597	−0.459	3.31E-04
P36955	Pigment epithelium-derived factor	133–141	−0.454	3.83E-04
Q9UHG2	ProSAAS	14–24	−0.444	5.42E-04
P09486	Secreted protein acidic and rich in cysteine	124–133	−0.523	3.01E-05
P09486	Secreted protein acidic and rich in cysteine	156–164	−0.477	1.75E-04
P09486	Secreted protein acidic and rich in cysteine	252–262	−0.457	3.55E-04
Q92563	Testican-2	139–148	−0.424	1.03E-03
Q06418	Tyrosine-protein kinase receptor TYRO3	279–290	−0.438	1.04E-03
P19320	Vascular cell adhesion protein 1	581–590	0.430	9.35E-04

HAM/TSP, human T-cell leukemia virus-1 associated myelopathy/tropic spastic paraparesis.

Statistical analysis for screening severity grade marker candidates

To extract biomarker proteins showing stoichiometric increase/decrease in accordance with progression of HAM/TSP, numerical classes (0, 1, 2, and 3) were given to four clinically relevant severity groups (AC, HAM/TSP OMDS 1–3, 4–6, and 7–11, respectively) (see Table S1). Then quantitative correlation between severity classes and 68,077 peptide intensities was ranked with Pearson's correlation analysis. Peptides with the lowest 100 *P*-values (Table S2) were next subjected to protein identification analysis by 2D-LC/MS/MS, resulting in successful identification of 14 proteins derived from 16 peptides (Table 2). In addition to Pearson's correlation coefficients and *P*-values in Table 2, LC/MS-based quantitative profiles of 16 peptides were illustrated with box plots (Fig. 3). Compared to a traditional severity grade marker neopterin ($R = 0.4105$, $P = 1.12E\text{-}03$), any of identified proteins showed better potential to be utilized as CSF disease state biomarkers.

SPARC and VCAM-1 as HAM/TSP severity grade markers in plasma

To further narrow down the biomarker candidates and establish plasma-based less-invasive diagnostics, we examined plasma levels of the 14 proteins by ELISA assays measuring 71 training cases (Table 3). The results revealed that a couple of proteins, SPARC and VCAM1, showed the same correlation in plasma with CSF levels ($|R| > 0.4$ and $P < 0.05$) (Fig. 4A and B). Therefore, we attempted construction of the combination biomarker diagnostics using newly identified two proteins and HTLV-1 viral load, all of which are measurable from small volume of blood samples. In order to halt the progression of HAM/TSP and maintain better quality of life for patients, both early diagnosis of HAM/TSP onset and therapeutic intervention at appropriate time point are essential. On the basis of these clinical requirements, we made two logistic regression models which maximized area under the curve (AUC) of ROC curves comparing ACs with HAM/TSP patients (onset predictor; (1)) or

Figure 2. Summary of CSF proteome. (A) Evaluation of LC/MS-based quantification analysis. The relative concentrations of CXCL10 cytokine calculated by mass spectrometric analysis were compared to independent measurements by cytometric bead array (CBA). (B) Venn diagram of identified proteins in 57 CSF analyses. The Gene Ontology (GO) analysis using DAVID Bioinformatics Resources displayed enriched cellular components of CSF proteins in ACs (C) or HAM/TSP patients (D). The enriched biological functions of CSF proteins in ACs (E) or HAM/TSP patients (F) were also shown. Expression Analysis Systematic Explorer (EASE) enrichment scores were shown. CSF, cerebrospinal fluid; CXCL10, C-X-C motif chemokine 10; ACs, asymptomatic carriers; HAM/TSP, human T-cell leukemia virus-1 associated myelopathy/tropic spastic paraparesis.

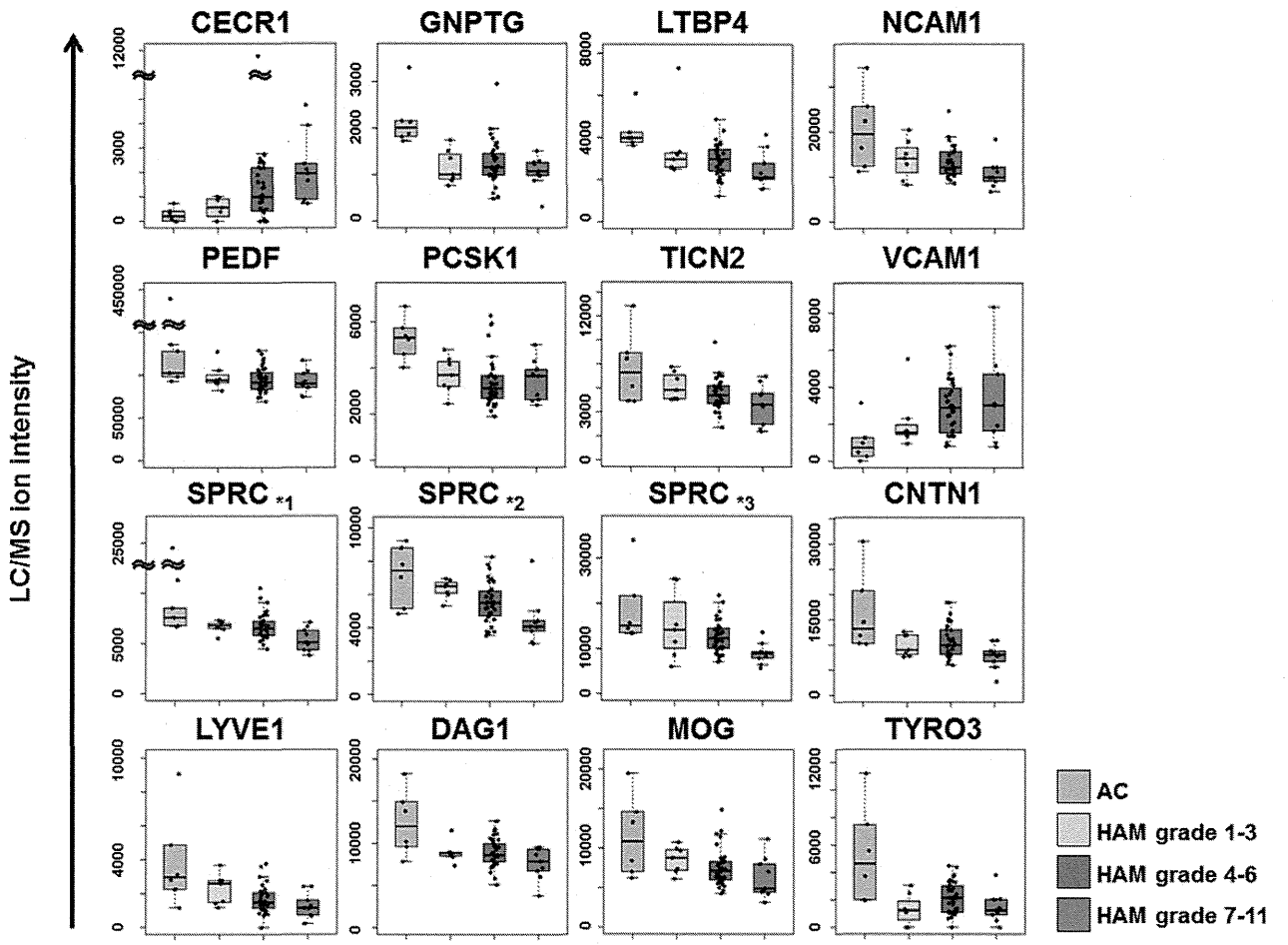

Figure 3. Panels of identified severity grade marker candidates for HAM/TSP. Box plots of 16 peptides derived from 14 candidate proteins are displayed. The Y axis stands for the LC/MS ion intensities. *1, *2, and *3 correspond to distinct SPARC-derived peptides. Amino acid numbers of peptides are as follows: *1; 124–133, *2; 156–164, *3; 252–262. HAM/TSP, human T-cell leukemia virus-1 associated myelopathy/tropic spastic paraparesis; SPARC, secreted protein acidic and rich in cysteine.

Table 3. Clinical characteristics of the plasma specimens.

Group	*N*	Age (±SD)	Gender (M/F)
Training cases			
AC	37	51.5 (±13.2)	13/24
HAM1_3	4	55.0 (±4.7)	3/1
HAM4_6	20	60.5 (±10.8)	4/16
HAM7_11	10	62.0 (±8.2)	2/8
Test cases			
AC	18	54.2 (±12.3)	4/14
HAM1_3	2	59.5 (±12.0)	0/2
HAM4_6	9	56.8 (±14.9)	4/5
HAM7_11	5	71.2 (±2.9)	0/5

AC, asymptomatic carriers; HAM1_3, HAM/TSP patients whose Osame's motor disability score range from 1 to 3; HAM4_6, HAM/TSP patients whose Osame's motor disability score range from 4 to 6; HAM7_11, HAM/TSP patients whose Osame's motor disability score range from 7 to 11.

ACs + HAM/TSP OMDS 1–3 with HAM/TSP OMDS 4–11 (therapeutic intervention predictor; (2)).

$$\log\left(\frac{P(x)}{1-P(x)}\right) = -11.19 - 0.01980\ (\text{SPARC}) + 0.009322\ (\text{VCAM1}) + 0.1142\ (\text{Viral Load}) \quad (1)$$

$$\log\left(\frac{P(x)}{1-P(x)}\right) = -11.73 - 0.01808\ (\text{SPARC}) + 0.009651\ (\text{VCAM1}) + 0.09151\ (\text{Viral Load}) \quad (2)$$

Finally, we assessed our prediction models using 105 plasma samples (71 training samples with 34 independent test samples). The AUC of ROC curves in Figure 4C and D demonstrated significantly higher diagnostic powers of our three-factor models for both onset prediction

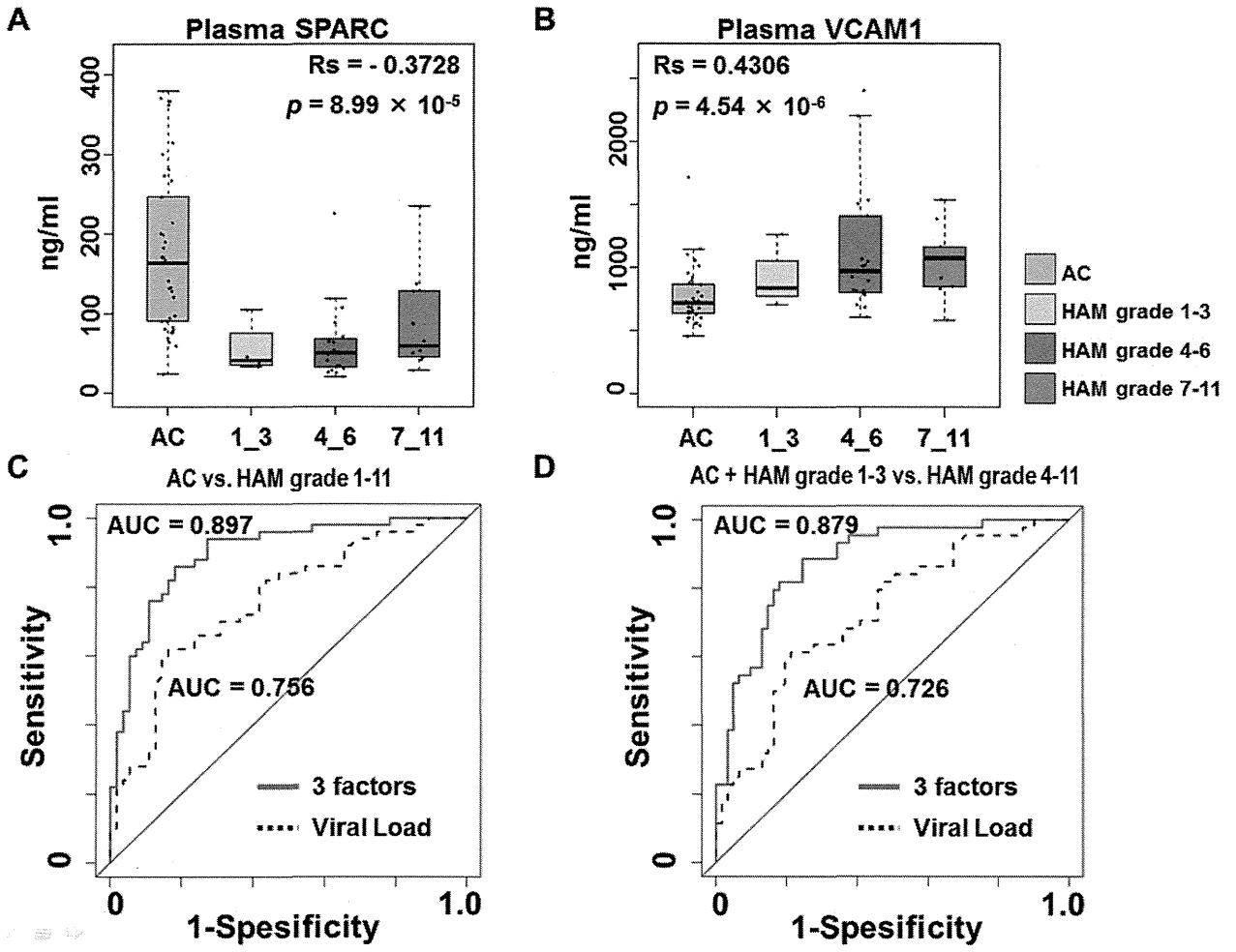

Figure 4. Construction of plasma-based diagnostic models. Plasma SPARC (A) and VCAM1 (B) were measured by ELISA assays. Pearson's correlation coefficient showed significant correlation between severity and novel markers. The three-factor logistic regression models (plasma SPARC, VCAM1, and HTLV-1 viral load) were validated with 105 samples in order for prediction of HAM/TSP onset (C) and appropriate therapeutic intervention point (D). The three-factor models showed better diagnostic performances than those of viral load only. Values of area under the curve (AUC) were shown. SPARC, secreted protein acidic and rich in cysteine; VCAM1, vascular cell adhesion molecule-1; ELISA, enzyme-linked immunosorbent assay; HTLV-1, human T-cell leukemia virus-1; HAM/TSP, human T-cell leukemia virus-1 associated myelopathy/ tropic spastic paraparesis.

(AUC = 0.897) and treatment initiation point prediction (AUC = 0.879), compared to two-factor models (AUC = 0.861 and 0.856, respectively), SPARC (AUC = 0.748 and 0.736, respectively), VCAM1 (AUC = 0.768 and 0.774, respectively), and HTLV-1 viral load (AUC = 0.756 and 0.726, respectively) (Figs. S2, S3). Additionally, sensitivity and specificity of three-factor model for onset prediction were 86.0% and 81.8%, respectively, whereas those for treatment initiation point prediction were 81.8% and 82.0%, respectively (Table 4). These diagnostic yields were significantly better than those of previously reported biomarkers CSF neopterin, CSF CXCL10, and serum soluble IL-2 receptor (sIL-2R) (Table S3). Thus, our three-factor diagnostics can provide valid and noninvasive routine test for HTLV-1 carriers and HAM/TSP patients, leading to precise disease control and better clinical outcome.

Discussion

An objective and scientifically evident diagnosis should be the basis of any medical actions. However, for HAM/TSP patients, clinical decisions have been made based on subjective health complaints mainly. Although HTLV-1 viral load, serum sIL-2R, and CSF neopterin are recently accepted as severity grade indicators for HAM/TSP,[5] only

Table 4. Prediction of HAM/TSP onset and the point of therapeutic intervention.

	Onset					Point of therapeutic intervention				
Predictors	3 factors	SPARC + VCAM1	SPARC	VCAM1	Viral load	3 factors	SPARC + VCAM1	SPARC	VCAM1	Viral load
Training set (n = 71)										
Sensitivity %	85.3	82.4	76.5	79.4	55.9	80.0	73.3	76.7	60.0	53.3
Specificity %	81.1	67.6	45.9	62.2	89.2	82.9	80.5	48.8	85.4	82.9
Positive predictive value %	80.6	70.0	56.5	65.9	82.6	77.4	73.3	52.3	75.0	69.6
Negative predictive value %	85.7	80.6	68.0	76.7	68.8	85.0	80.5	74.1	74.5	70.8
AUC	0.897	0.839	0.669	0.754	0.732	0.881	0.846	0.667	0.773	0.699
Test set (n = 105)										
Sensitivity %	86.0	88.0	82.0	80.0	62.0	81.8	79.5	81.8	56.8	61.4
Specificity %	81.8	69.1	49.1	63.6	83.6	82.0	80.3	54.1	82.0	78.7
Positive predictive value %	81.1	72.1	59.4	66.7	77.5	76.6	74.5	56.3	69.4	67.5
Negative predictive value %	86.5	86.4	75.0	77.8	70.8	86.2	84.5	80.5	72.5	73.8
AUC	0.897	0.861	0.748	0.768	0.756	0.879	0.856	0.736	0.774	0.726

3 factors, logistic regression model using SPARC, VCAM1, and HTLV-1 viral load; HAM/TSP, human T-cell leukemia virus-1 associated myelopathy/tropic spastic paraparesis; AUC, area under the curve of ROC analysis.

relative increase/decrease of these biomarkers is valuable to assess efficiency of treatment. In this study, we successfully established predictive models which quantitatively define HAM/TSP disease status directly from plasma SPARC, VCAM1, and HTLV-1 viral load. This three-factor prediction model can be easily involved in routine medical examinations for ACs to monitor HAM/TSP onset because three biomarkers are measurable from a single blood collection without any invasive procedures such as CSF collection. Because progression of HAM/TSP tends to be rapid typically within a few years since the onset,[12] our prediction model for treatment initiation point will effectively prevent delay of deciding therapeutic intervention for early stage HAM/TSP patients.

Concerning physiological consideration of a new biomarker SPARC, the expression is specifically restricted within glial cells in nervous system including spinal cord.[13] In addition, encephalitis induced by *N*-methyl-D-aspartic acid (NMDA) in mice resulted in downregulation of SPARC in glial cells.[14] These facts suggested that plasma level of SPARC in HAM/TSP patients decrease along with the diminished number of glial cells caused by spinal cord degeneration and reduced expression of SPARC in glial cells which are pathological characteristics of HAM/TSP. On the other hand, CSF neopterin is known as an inflammatory small biological compound upregulated in many inflammatory neurologic diseases, such as multiple sclerosis, HIV encephalopathy, and Lyme neuroborreliosis,[15–17] indicating that neopterin cannot describe spinal cord degeneration specifically. Therefore, SPARC in plasma or CSF can be considered as more specific biomarker for HAM/TSP compared to CSF neopterin. Another new biomarker VCAM1 is expressed on the surface of endothelial cells, whose soluble form is known to be upregulated in plasma during the process of inflammation.[18] In HAM/TSP patients, VCAM1 is upregulated in inflammatory region within spinal cord.[19] Hence, diagnostic features of VCAM1 are more disease-oriented than neopterin, but VCAM1 can be measured from noninvasive blood specimens.

In conclusion, proteome-wide quantitative profiling of CSFs identified 14 severity grade biomarkers for HAM/TSP. Two of them, SPARC and VCAM1, were confirmed to be useful for plasma-based diagnosis of HAM/TSP onset and severity grades. It has long been difficult to expect a sudden onset of HAM/TSP after decades of asymptomatic phase in 0.5% of HTLV-1 carriers. Routine examination of our triple biomarkers will contribute to early diagnosis of HAM/TSP, leading to appropriate management of disease before suffering severe symptoms.

Acknowledgment

This work was supported by grant-in-aid for Research Project on Overcoming Intractable Diseases from the Ministry of Health Labour and Welfare Japan and grant-in-aid for Young Scientists (B) (23701090) from the Ministry of Education, Culture, Sports, Science & Technology Japan.

Conflict of Interest

Dr. Ueda has a patent Methods for detection and disease stage classification of HTLV-1 associated myelopathy pending. Dr. Ishihara has a patent Methods for detection and disease stage classification of HTLV-1 associated myelopathy pending. Dr. Araya has a patent Methods for detection and disease stage classification of HTLV-1 associated myelopathy pending. Dr. Saichi has a patent Methods for detection and disease stage classification of HTLV-1 associated myelopathy pending. Dr. Fujii has a patent Methods for detection and disease stage classification of HTLV-1 associated myelopathy pending. Dr. Sugano has a patent Methods for detection and disease stage classification of HTLV-1 associated myelopathy pending. Dr. Sato has a patent Methods for detection and disease stage classification of HTLV-1 associated myelopathy pending. Dr. Yamano has a patent Methods for detection and disease stage classification of HTLV-1 associated myelopathy pending.

References

1. Yamashita M, Ido E, Miura T, Hayami M. Molecular epidemiology of HTLV-I in the world. J Acquir Immune Defic Syndr Hum Retrovirol 1996;13(suppl 1):S124–S131.
2. Asquith B, Zhang Y, Mosley AJ, et al. In vivo T lymphocyte dynamics in humans and the impact of human T-lymphotropic virus 1 infection. Proc Natl Acad Sci USA 2007;104:8035–8040.
3. Enose-Akahata Y, Abrams A, Johnson KR, et al. Quantitative differences in HTLV-I antibody responses: classification and relative risk assessment for asymptomatic carriers and ATL and HAM/TSP patients from Jamaica. Blood 2012;119:2829–2836. doi: 10.1182/blood-2011-11-390807
4. Franzoi AC, Araujo AQ. Disability and determinants of gait performance in tropical spastic paraparesis/HTLV-I associated myelopathy (HAM/TSP). Spinal Cord 2007;45:64–68.
5. Yamano Y, Sato T. Clinical pathophysiology of human T-lymphotropic virus-type 1-associated myelopathy/tropical spastic paraparesis. Front Microbiol 2012;3:389. doi: 10.3389/fmicb.2012.00389
6. Kannagi M, Harashima N, Kurihara K, et al. Tumor immunity against adult T-cell leukemia. Cancer Sci 2005;96:249–255.
7. Shublaq M, Orsini M, Puccioni-Sohler M. Implications of HAM/TSP functional incapacity in the quality of life. Arq Neuropsiquiatr 2011;69(2A):208–211.
8. Semmes OJ, Cazares LH, Ward MD, et al. Discrete serum protein signatures discriminate between human retrovirus-associated hematologic and neurologic disease. Leukemia 2005;19:1229–1238.
9. Kirk PD, Witkover A, Courtney A, et al. Plasma proteome analysis in HTLV-1-associated myelopathy/tropical spastic paraparesis. Retrovirology 2011;8:81. doi: 10.1186/742-4690-8-81
10. Rahman S, Quann K, Pandya D, et al. HTLV-1 Tax mediated downregulation of miRNAs associated with chromatin remodeling factors in T cells with stably integrated viral promoter. PLoS One 2012;7:e34490. doi: 10.1371/journal.pone.0034490
11. Pepe MS, Cai T, Longton G. Combining predictors for classification using the area under the receiver operating characteristic curve. Biometrics 2006;62:221–229.
12. Taylor GP, Goon P, Furukawa Y, et al. Zidovudine plus lamivudine in human T-lymphotropic virus type-I-associated myelopathy: a randomised trial. Retrovirology 2006;3:63.
13. Vincent AJ, Lau PW, Roskams AJ. SPARC is expressed by macroglia and microglia in the developing and mature nervous system. Dev Dyn 2008;237:1449–1462.
14. Lloyd-Burton SM, York EM, Anwar MA, et al. SPARC regulates microgliosis and functional recovery following cortical ischemia. J Neurosci 2013;33:4468–4481.
15. Fredrikson S, Link H, Eneroth P. CSF neopterin as marker of disease activity in multiple sclerosis. Acta Neurol Scand 1987;75:352–355.
16. Karlsen NR, Froland SS, Reinvang I. HIV-related neuropsychological impairment and immunodeficiency. CD8+ lymphocytes and neopterin are related to HIV-encephalopathy. Scand J Psychol 1994;35:230–239.
17. Gasse T, Murr C, Meyersbach P, et al. Neopterin production and tryptophan degradation in acute Lyme neuroborreliosis versus late Lyme encephalopathy. Eur J Clin Chem Clin Biochem 1994;32:685–689.
18. Devaraj S, Glaser N, Griffen S, et al. Increased monocytic activity and biomarkers of inflammation in patients with type 1 diabetes. Diabetes 2006;55:774–779.
19. Izumo S. Neuropathology of HTLV-1-associated myelopathy (HAM/TSP). Neuropathology 2010;30:480–485.

Supporting Information

Additional Supporting Information may be found in the online version of this article:

Table S1. Osame's Motor Disability Score (OMDS).
Table S2. List of peptides with the lowest 100 *P*-values.
Table S3. Prediction of HAM/TSP onset and point of therapeutic intervention with existing markers.
Figure S1. Data acquired in LC/MS/MS analyses were loaded on Refiner MS and 2D-planes represented by mass-to-charge ratio and retention time were generated. To eliminate peaks originated from chemical noises on 2D-planes, four-step Noise Subtraction was conducted. All samples were aligned by retention times and 2D-planes

were merged into a single plane to determine peptide-derived peaks in Summed Peak Detection algorithm. Quantitative information accompanying each peptide was extracted after isotope clustering and statistical analyses were performed.

Figure S2. The classifiers for HAM/TSP onset established with two factors, SPARC and VCAM1 were appraised by area under the curve of ROC curve. Red lines indicate the ROC curves of (A) two factors, (B) SPARC, and (C) VCAM1. Black broken lines show ROC curve of viral load.

Figure S3. The classifiers which distinguished HAM 4–11 from the others were evaluated by AUC. Red lines indicate ROC curves of (A) two factors, (B) SPARC, and (C) VCAM1. Black broken lines indicate viral load.

nature COMMUNICATIONS

ARTICLE

Received 5 Mar 2014 | Accepted 29 Oct 2014 | Published 9 Dec 2014

DOI: 10.1038/ncomms6691 OPEN

Critical role of lysine 134 methylation on histone H2AX for γ-H2AX production and DNA repair

Kenbun Sone[1], Lianhua Piao[1], Makoto Nakakido[1], Koji Ueda[2], Thomas Jenuwein[3], Yusuke Nakamura[1] & Ryuji Hamamoto[1,4]

The presence of phosphorylated histone H2AX (g-H2AX) is associated with the local activation of DNA-damage repair pathways. Although g-H2AX deregulation in cancer has previously been reported, the molecular mechanism involved and its relationship with other histone modifications remain largely unknown. Here we find that the histone methyltransferase SUV39H2 methylates histone H2AX on lysine 134. When H2AX was mutated to abolish K134 methylation, the level of g-H2AX became significantly reduced. We also found lower g-H2AX activity following the introduction of double-strand breaks in Suv39h2 knockout cells or on SUV39H2 knockdown. Tissue microarray analyses of clinical lung and bladder tissues also revealed a positive correlation between H2AX K134 methylation and g-H2AX levels. Furthermore, introduction of K134-substituted histone H2AX enhanced radio- and chemosensitivity of cancer cells. Overall, our results suggest that H2AX methylation plays a role in the regulation of g-H2AX abundance in cancer.

[1] Section of Hematology/Oncology, Department of Medicine, University of Chicago, 5841 South Maryland Avenue, MC2115, Chicago, Illinois 60637, USA. [2] Graduate School of Frontier Sciences, The University of Tokyo, 4-6-1 Shirokanedai, Minato-ku, Tokyo 108-8639, Japan. [3] Max Planck Institute of Immunobiology and Epigenetics, Stübeweg 51, D-79108 Freiburg, Germany. [4] Laboratory of Molecular Medicine, Human Genome Center, Institute of Medical Science, University of Tokyo, 4-6-1 Shirokanedai, Minato-ku, Tokyo 108-8639, Japan. Correspondence and requests for materials should be addressed to R.H. (email: rhamamoto@medicine.bsd.uchicago.edu).

The structural subunit of chromatin is the nucleosome, which consist of a histone octameric core constituted of four different histone types: H2A, H2B, H3 and H4. These nuclear histones can undergo a variety of chemical modifications such as acetylation, methylation, ubiquitination, sumoylation, poly ADP-ribosylation and phosphorylation[1]. The combination of these dynamic modifications form the so-called 'histone code', which influences gene expression, the DNA-damage response (DDR) and DNA repair[2,3]. Histone H2AX is a member of the histone H2A family and accounts for ~10% of total H2A molecules in normal human fibroblasts. However, the amounts of H2AX significantly vary between cell types[4–6]. H2AX plays a critical role in the DDR following induction of double-strand breaks (DSBs). When DSBs occur, H2AX accumulates near the DNA breakage sites and is quickly phosphorylated by members of the phosphatidyl-inositol-3-kinase-related kinases family, including ataxia telangiectasia-mutated (ATM), ataxia telangiectasia and Rad3-related (ATR) and DNA-activated protein kinase[7]. This phosphorylated form of histone H2AX is referred to as **g**-H2AX and is a marker of DNA damage. **g**-H2AX accumulates at sites of damaged chromatin within seconds of the formation of a DSB and triggers the accumulation of several components involved in the DDR signalling cascade[8,9]. In addition to phosphorylation, ubiquitination of H2AX has also been reported[10]. Several studies have highlighted the functions of RING finger ubiquitin ligases, RNF2, RNF8 and RNF168, in promoting accumulation of repair proteins at DSBs in an MDC1 (mediator of DNA-damage checkpoint protein 1)-dependent manner[11–14]. A number of *in vitro* and *in vivo* studies have demonstrated that phosphorylation and ubiquitination of H2AX play a central role in regulating various cellular responses to DSBs, including DNA repair and cell cycle checkpoints[15,16]. Furthermore, as DSBs are the most deleterious DNA damages that cause genomic instability and enhance the risk of tumorigenesis, deregulation of **g**-H2AX seems to be linked to human cancer[17,18].

Suppressor of Variegation 3–9 Homologue 2 (SUV39H2), also known as KMT1B[19], is a SET-domain-containing methyltransferase that selectively methylates H3K9. The expression of *Suv39h2*—the murine homologue of human *SUV39H2*—is restricted to the testis in adult tissues and the endogenous Suv39h2 protein was shown to be enriched at heterochromatin during the first meiotic prophase and in the early stages of spermatogenesis. During mid-pachytene, Suv39h2 specifically accumulates with chromatin of the silenced sex chromosomes present in the XY body. In addition, Suv39h2 histone methyltransferase activity appears to play an important role in regulating higher-order chromatin dynamics during male meiosis[20]. On the other hand, the biological significance of SUV39H2 deregulation in human tumorigenesis is almost unknown. In the present study, we demonstrate that SUV39H2 methylates histone H2AX, and that the H2AX methylation is critical for **g**-H2AX accumulation in human cancer.

Results

SUV39H2 methylates H2AX and is overexpressed in cancer. To investigate the possible function of methylation in the regulation of H2AX, we conducted *in vitro* methyltransferase assays against H2AX using a variety of histone methyltransferases. SUV39H2, a SET-domain-containing histone methyltransferase reported to methylate H3K9 (refs 20,21), was found to be able to methylate histone H2AX (Fig. 1a). The histone methyltransferase activity of SUV39H2 appears to play an important role in regulating chromatin structure and dynamics, whereas the biological significance of SUV39H2 deregulation in human tumorigenesis is still largely unexplored. Hence, we investigated the role of SUV39H2 and its relation to H2AX modification in human cancers.

We first examined expression levels of *SUV39H2* in 16 normal and 14 lung cancer tissues (9 non-small-cell lung carcinoma (NSCLC) cases and 5 SCLC cases) using quantitative real-time PCR analysis, and found that *SUV39H2* was significantly upregulated in cancer cells compared with that in normal tissues (Fig. 1b,c). We subsequently conducted immunohistochemical analysis of SUV39H2 in lung cancer and normal tissues, and found that SUV39H2 was overexpressed in 217 out of 328 archival NSCLC cases in accordance with the Oncomine database, while no staining was observed in normal organs, except for the testis (Fig. 1d,e). Expression profile analysis by complementary DNA microarray using a large number of clinical cases also revealed overexpression of *SUV39H2* in cervical, bladder, oesophageal and prostate cancers, as well as in osteosarcomas and soft tissue sarcomas (Supplementary Table 1).

SUV39H2 is critical for chemo- and radiosensitivity. To investigate the role of SUV39H2 in human cancer and the relationship between SUV39H2 and **g**-H2AX, we examined the effect of SUV39H2 knockdown on radio- and chemosensitivity of cancer cells, because **g**-H2AX is considered as a key regulator of the DNA repair system after DSBs, which causes chemo/radio-resistance of cancer cells[6]. The lung squamous carcinoma RERF-LC-AI cells overexpressing SUV39H2 (Supplementary Fig. 1) was treated with control small interfering RNA (siRNA) or two different siRNAs directed to SUV39H2 for 48 h, followed by irradiation with 3 or 6 Gy of ionizing radiation. Subsequent cell viability analysis revealed that SUV39H2 knockdown enhanced the sensitivity of RERF-LC-AI cells to radiation (Supplementary Fig. 2a). We also examined the effect of SUV39H2 knockdown on chemosensitivity. RERF-LC-AI cells were transfected with control siRNA and either of two independent SUV39H2 siRNAs, and then treated with various concentrations of cisplatin or doxorubicin 48 h after siRNA transfection. Cell viability IC50 values after 48 h cisplatin treatment were calculated to be ~10 **n**M for the control siRNA, and 0.38 **n**M and 0.21 **n**M for siSUV39H1#1 and siSUV39H1#2, respectively. Those for the doxorubicin treatment were 2.21 **n**M for the control siRNA, and 0.096 and 0.066 **n**M for siSUV39H1#1 and siSUV39H1#2, respectively (Supplementary Fig. 2b), further supporting SUV39H2 as playing a role in chemosensitivity.

Lysine 134 on histone H2AX is dimethylated by SUV39H2. We next examined the relationship between SUV39H2-dependent histone H2AX methylation and **g**-H2AX production. We first performed liquid chromatography-tandem mass spectrometry (MS/MS) to identify the site of methylation for histone H2AX, and found that lysine 134 was dimethylated by SUV39H2 (Fig. 2a). To validate this result, we prepared recombinant H2AX-K134A—where lysine 134 is substituted for alanine—and performed an *in vitro* methyltransferase assay (Fig. 2b). The intensity of the band corresponding to histone H2AX methylation was significantly diminished in the K134A mutant compared with that of wild-type H2AX (H2AX-WT), suggesting that lysine 134 of histone H2AX is a novel substrate of SUV39H2. Lysine 134 is located in a peptide region unique to H2AX among the H2A family members and is located near serine 139. Ser139-phosphorylated H2AX is known as **g**-H2AX (Fig. 2c). As lysine 134 is highly conserved from *Danio rerio* to *Homo sapiens*, we postulated that methylation of this site might be critical for the regulation of histone H2AX functions and the production of **g**-H2AX (Fig. 2d).

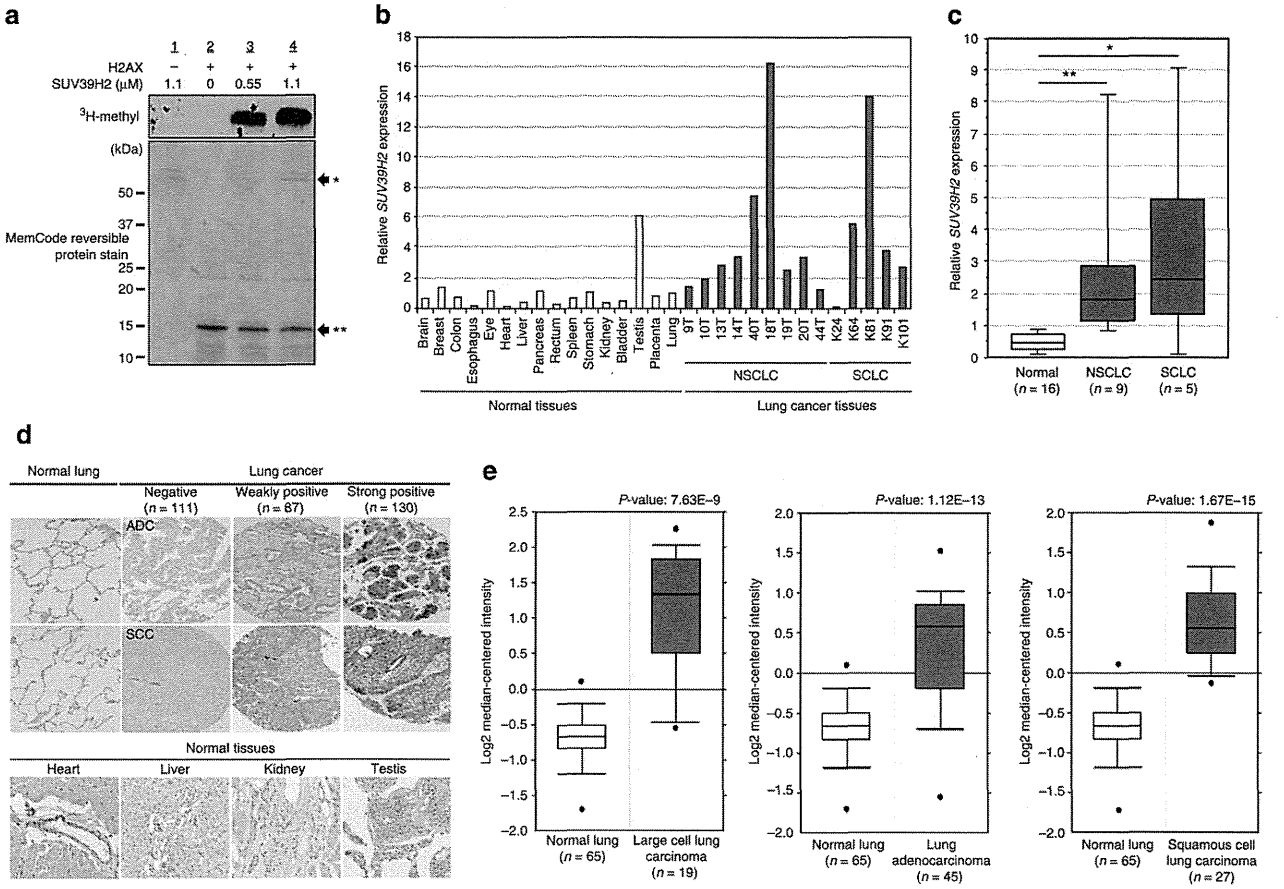

Figure 1 | SUV39H2 is overexpressed in human lung cancer. (**a**) *In vitro* methyltransferase analysis of SUV39H2. Recombinant histone H2AX and ^{3}H-SAM were incubated in the presence or absence of recombinant SUV39H2, and the reaction products were analysed by SDS-PAGE followed by fluorography (upper panel) and stained for total protein(lower panel). (**b**) *SUV39H2* mRNA levels in 14 lung cancer cases (NSCLC: 9 cases; SCLC: 5 cases) and 16 normal tissues. (**c**) Quantitative real-time PCR analysis was performed in 14 lung cancer samples and 16 normal tissues (the brain, breast, colon, oesophagus, eye, heart, liver, pancreas, rectum, spleen, stomach, kidney, bladder, testis, placenta and lung) and the result is shown by box-whisker plot. For statistical analysis, Kruskal–Wallis ($^{*}P<0.05$) and Student's *t*-test ($^{**}P<0.05$) were performed. (**d**) Representative cases for positive SUV39H2 expression in lung cancer tissues and normal adult tissues. ADC, adenocarcinoma; SCC, squamous cell carcinoma. Original magnification, ×100 (lung ×200). (**e**) Expression levels of *SUV39H2* in 65 normal lung samples, 19 large cell lung carcinoma samples, 45 lung adenocarcinoma samples and 27 squamous cell lung carcinoma samples. SUV39H2 is overexpressed in all three types of lung cancer. Expression profile is derived from Oncomine database.

To investigate this possibility, we generated an antibody against a synthetic peptide containing dimethylated K134 and confirmed its affinity and specificity by enzyme-linked immunosorbent assay (Fig. 2e). To verify the quality of the H2AX K134-methylation antibody, we prepared both H2AX-WT and H2AX-K134A recombinant proteins, and performed *in vitro* methyltransferase assays using recombinant SUV39H2 protein as an enzyme source. The methylation signal of H2AX-WT was clearly observed in the presence of SUV39H2, while the signal was absent when H2AX-K134A protein was used as a substrate (Fig. 2f). Using this antibody, we performed immunocytochemical analysis after transfection of a SUV39H2 expression vector into HeLa cells, to further verify SUV39H2-dependent H2AX K134 methylation *in vivo*, and detected a strong staining of K134-methylated H2AX in SUV39H2-overexpressing HeLa cells (Fig. 2g). Furthermore, we expressed FLAG-H2AX-WT or a FLAG-H2AX K134A, along with an influenza hemagglutinin (HA) control or HA-SUV39H2, into 293T cells. Western blot analysis of FLAG-immunoprecipitated protein with anti-K134-methylated H2AX exhibited a specific signal when both H2AX-WT and SUV39H2 proteins were co-expressed, but no signal was detected in H2AX K134A mutant (Fig. 2h). Taken together, these data indicate that SUV39H2 methylates histone H2AX on lysine 134 both *in vitro* and *in vivo*.

H2AX K134 methylation is critical for γ-H2AX production. To examine the physiologic significance of H2AX K134 methylation for **g**-H2AX production, we transfected either of siNegative control (siNC; control), siEGFP (control), SUV39H2-siRNA#1 or SUV39H2-siRNA#2 into RERF-LC-AI cells. Forty-eight hours after transfection, the cells were treated with 1 **m**M doxorubicin for 2 h. Western blot analysis detected high levels of **g**-H2AX in the cells treated with the control siRNAs, but significantly less **g**-H2AX was present when the cells were pre-treated with siSUV39H2s (Fig. 3a,b). The observed decrease in **g**-H2AX production following SUV39H2 knockdown appeared not to be caused by changes in quantity or activity of ATM and ATR kinases, as the amounts of ATM and ATR—responsible for H2AX serine 139 phosphorylation—as well as those of phospho-ATM (active-form of ATM) and phospho-Chk2 (Checkpoint kinase 2, a substrate of ATM and ATR) were unchanged. Importantly, given that the suppression of H2AX K134 dimethylation following knockdown of SUV39H2 was clearly observed in the endogenous H2AX proteins after immunoprecipitation (IP) with an H2AX antibody (Fig. 3c), SUV39H2 appears to be a fundamental regulator of endogenous H2AXK134 dimethylation. In addition, we confirmed that doxorubicin-induced DSBs did not affect SUV39H2 expression and H2AX K134 methylation

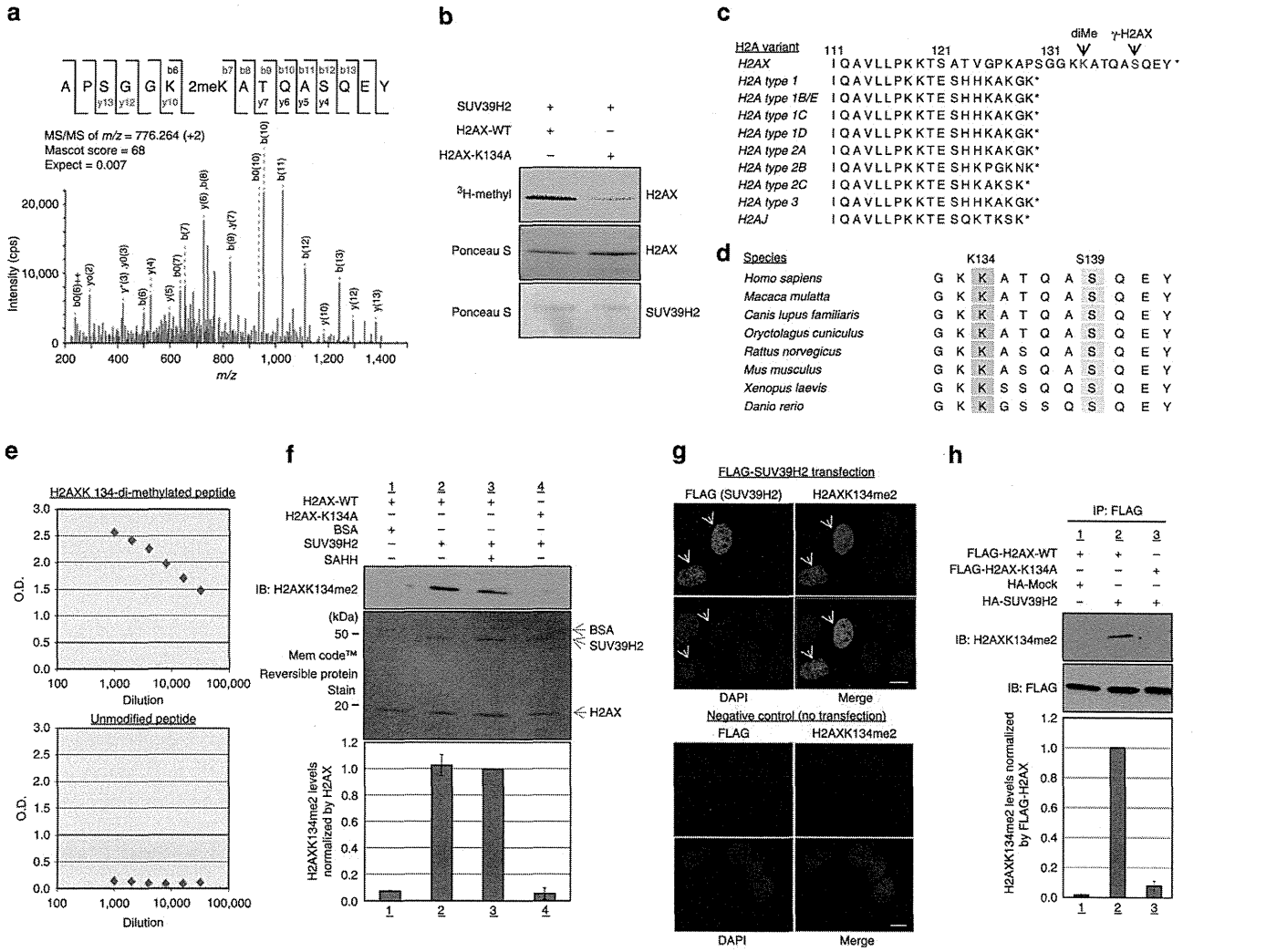

Figure 2 | SUV39H2 methylates lysine 134 on histone H2AX both *in vitro* and *in vivo*. (**a**) The MS/MS spectrum corresponding to the dimethylated histone H2AX peptide (residues 128–142). A 28-Da increase indicates dimethylated Lys 134. Score and Expect show Mascot Ion Score and Expectation value in Mascot Database search results are shown, respectively. (**b**) Validation of K134 methylation on histone H2AX. Recombinant histone H2AX-WT or H2AX-K134A proteins and ^{3}H-SAM were incubated in the presence of recombinant SUV39H2, and the reaction products were analysed by SDS–PAGE followed by fluorography. The membrane was stained with Ponceau S (lower panel). (**c**) Amino acid sequence alignment of human histone H2A family. Lysine 134 is located in the unique sequence portion of H2AX. (**d**) Amino acid sequence alignment of H2AX unique sequence portion. (**e**) Determination of the titre and specificity of the anti-dimethylated K134 H2AX antibody analysed by enzyme-linked immunosorbent assay. (**f**) Validation of the anti-dimethylated K134 H2AX antibody. Recombinant H2AX-WT or H2AX-K134A proteins and SAM were incubated in the presence or absence of recombinant SUV39H2, and the reaction products were analysed by WB analysis. The intensity of each H2AX K134 dimethylation signal was normalized by the corresponding H2AX. SAHH, *S*-adenosyl-L-homocysteine hydrolase. Results are the mean ± s.d. ($n = 3$). (**g**) Immunocytochemical analysis of HeLa cells. Cells were stained with an anti-FLAG antibody (green), an anti-H2AX K134me2 antibody (red) and 4′,6-diamidino-2-phenylindole dihydrochloride (DAPI (blue)). Non-transfected HeLa cells were used as negative control. Scale bars, 10 μm. (**h**) 293T cells were co-transfected with a FLAG-H2AX-WT or a FLAG-H2AX-K134A, and an empty vector (HA-Mock) or HA-SUV39H2. The samples were immunoblotted with anti-dimethylated K134 H2AX and anti-FLAG antibodies following IP with anti-FLAG. Results are the mean ± s.d. ($n = 3$).

levels (Fig. 3d). To validate the effect of SUV39H2 on γ-H2AX production, we performed immunocytochemical analysis using the anti-γ-H2AX antibody and detected significant decrease of γ-H2AX levels following knockdown of SUV39H2 (Fig. 3e,f), consistent with the western blotting (WB) results. These data suggest that SUV39H2 plays a critical role in γ-H2AX activation. We next prepared *Suv39h2*-null (*Suv39h2*$^{-/-}$) mouse embryonic fibroblast (MEF) cells from *Suv39h2* knockout mouse[22], to confirm the knockdown experiments. Both *Suv39h2*$^{-/-}$ and *Suv39h2*-WT MEFs were treated with 1 μM doxorubicin for 2 h before lysis. Western blot analysis confirmed significantly lower levels of γ-H2AX activity in *Suv39h2*$^{-/-}$ MEFs compared with that in Suv39h2-WT MEFs (Supplementary Fig. 3). Moreover, we examined laser-induced γ-H2AX activity in *Suv39h2*$^{-/-}$ and *Suv39h2*-WT MEFs, and confirmed that *Suv39h2*$^{-/-}$ cells showed reduced γ-H2AX compared with *Suv39h2*-WT cells (Supplementary Fig. 4).

To further evaluate the effect of H2AX K134 methylation on γ-H2AX production *in vivo*, we co-expressed FLAG-H2AX-WT or FLAG-H2AX-K134A with HA-SUV39H2 in HeLa cells before treatment with doxorubicin. IP and WB analysis show that γ-H2AX was induced to a higher level in the presence of H2AX-WT, compared with two H2AX-K134A or K134R (Fig. 4a,b and Supplementary Fig. 5). In addition, we found that the amount of phospho-ATM and ATR bound to H2AX were decreased in K134-substituted H2AX. Furthermore, we co-expressed

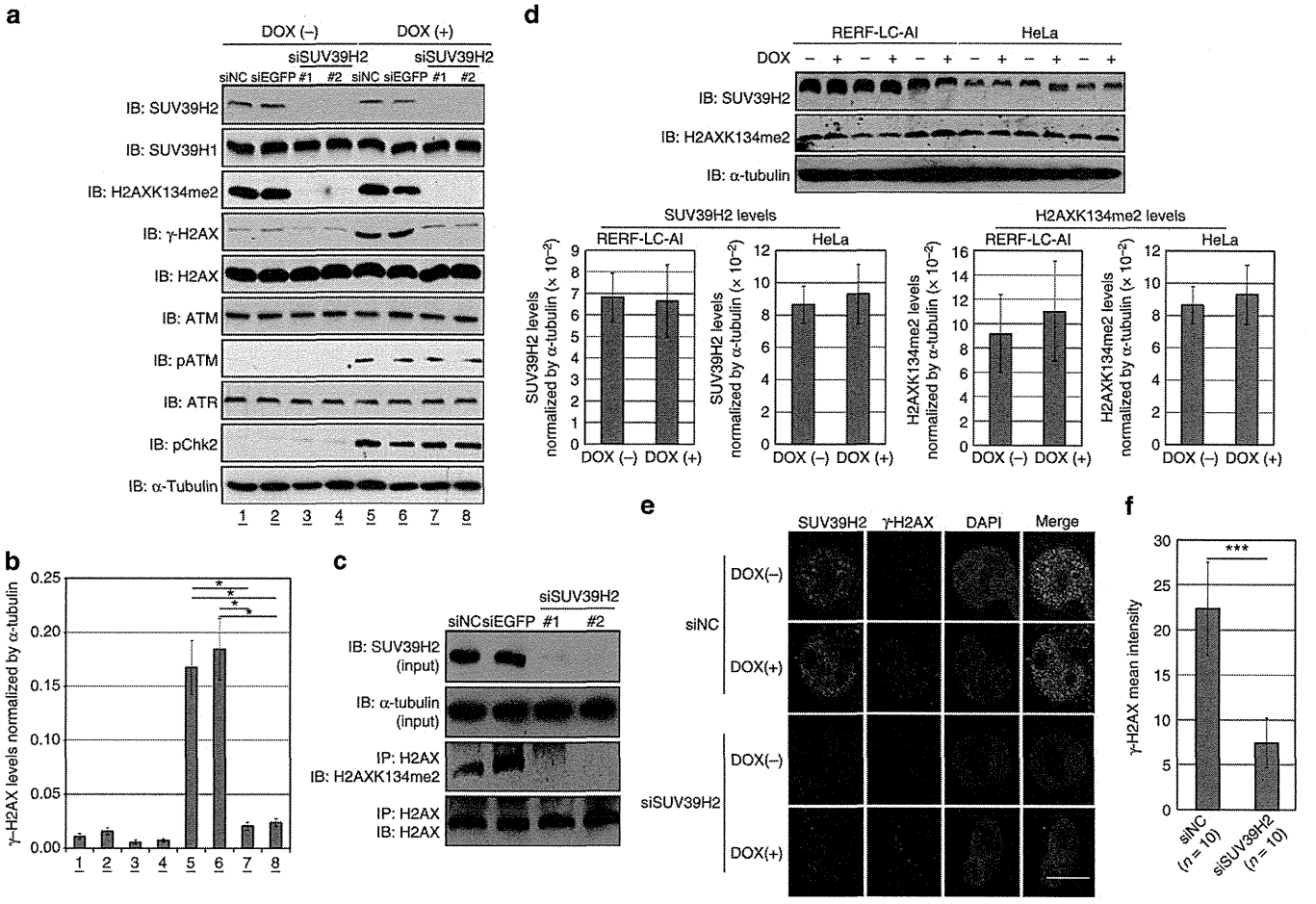

Figure 3 | SUV39H2 is critical for γ-H2AX production. (**a**) Effects of SUV39H2 knockdown on the γ-H2AX levels. RERF-LC-AI cells were transfected with two control siRNAs (siNC and siEGFP) and SUV39H2 siRNAs (#1 and #2), and were treated with 1 μM of doxorubicin 48 h after transfection with siRNAs. Cells were harvested 2 h after treatment with doxorubicin, followed by SDS-PAGE. Western blotting was performed using anti-SUV39H2, anti-SUV39H1, anti-dimethylated K134 H2AX, anti-γ-H2AX, anti-H2AX, anti-phospho-ATM, anti-ATM, anti-ATR, anti-phosph-Chk2 and anti-α-Tubulin (internal control) antibodies. (**b**) The intensity of γ-H2AX levels was normalized by α-Tubulin and averaged. Results are the mean ± s.d. ($n = 3$). *P*-values were calculated using Student's *t*-test (*$P < 0.05$). (**c**) RERF-LC-AI cells were transfected with two control siRNAs (siNC and siEGFP) and SUV39H2 siRNAs (#1 and #2), and were treated with 1 μM of doxorubicin 48 h after transfection with siRNAs. Cells were harvested 2 h after treatment with doxorubicin and IP was conducted using an anti-H2AX antibody. Input and immunoprecipitated samples were immunoblotted with anti-SUV39H2, anti-α-Tubulin, anti-dimethylated K134 H2AX and anti-H2AX antibodies. (**d**) RERF-LC-AI and HeLa cells were treated with 1 μM of doxorubicin for 2 h before lysis. The samples were immunoblotted with anti-SUV39H2, anti-H2AXK134me2 and anti-α-Tubulin antibodies. The intensity of SUV39H2 and H2AK134me2 levels was normalized by α-Tubulin expression levels. Results are the mean ± s.d. ($n = 3$). (**e**) Immunocytochemical analysis of RERF-LC-AI cells. Cells were transfected with control siRNA and SUV39H2 siRNA, and were treated with 1 μM of doxorubicin 48 h after transfection with siRNAs for 1 h. Cells were stained with an anti-SUV39H2 antibody (green), an anti-γ-H2AX antibody (red) and 4′,6-diamidino-2-phenylindole dihydrochloride (DAPI (blue)) 2 h after treatment with doxorubicin. Scale bar, 10 μm. (**f**) γ-H2AX intensity examined in **e** was quantified with the Image J software and averaged. Results are the means ± s.d. of ten independent cells. *P*-values were calculated using Student's *t*-test (***$P < 0.001$).

H2AX-WT or H2AX-K134A with SUV39H2 in $H2AX^{-/-}$ MEFs to validate the relationship between H2AX K134 methylation and γ-H2AX production. First, we confirmed that overexpressed H2AX-WT and H2AX-K134A were appropriately incorporated into chromatin of $H2AX^{-/-}$ MEF cells by immunocytochemistry (ICC; Supplementary Fig. 6), and then conducted WB analysis following purification of the chromatin fraction (Supplementary Fig. 7). γ-H2AX production in $H2AX^{-/-}$ MEF cells overexpressing H2AX-K134A was clearly suppressed compared with $H2AX^{-/-}$ MEF cells overexpressing H2AX-WT, confirming the critical role of H2AX K134 dimethylation in γ-H2AX production.

To explore the relationship between H2AX K134 methylation and H2AX S139 phosphorylation in more detail, we prepared biotin-conjugated unmodified H2AX and K134 dimethylated H2AX peptides encompassing amino acids 121–142 (Fig. 4c), and conducted *in vitro* kinase and pull-down assays. Biotin-conjugated peptides were mixed with lysates from HeLa cells treated with doxorubicin and pulled down with Dynabeads M-280 streptavidin followed by WB analysis (Fig. 4c,d). The K134 dimethylated H2AX peptide exhibited a much higher level of H2AX S139 phosphorylation than the unmodified H2AX peptide. We also observed that the amount of phospho-ATM and ATR bound to the K134-dimethylated H2AX peptide was significantly higher compared with the unmodified peptide, consistent with the above data (Fig. 4e). Moreover, we also conducted the *in vitro* kinase assay of H2AX peptides using immunoprecipitated ATM as the source of enzyme (Fig. 4f). The K134-dimethylated peptide showed notably higher H2AX S139 phosphorylation compared with the unmodified and K134R peptides (Fig. 4g). In addition, KU-55933, an ATM kinase inhibitor, diminished H2AX S139 phosphorylation of the

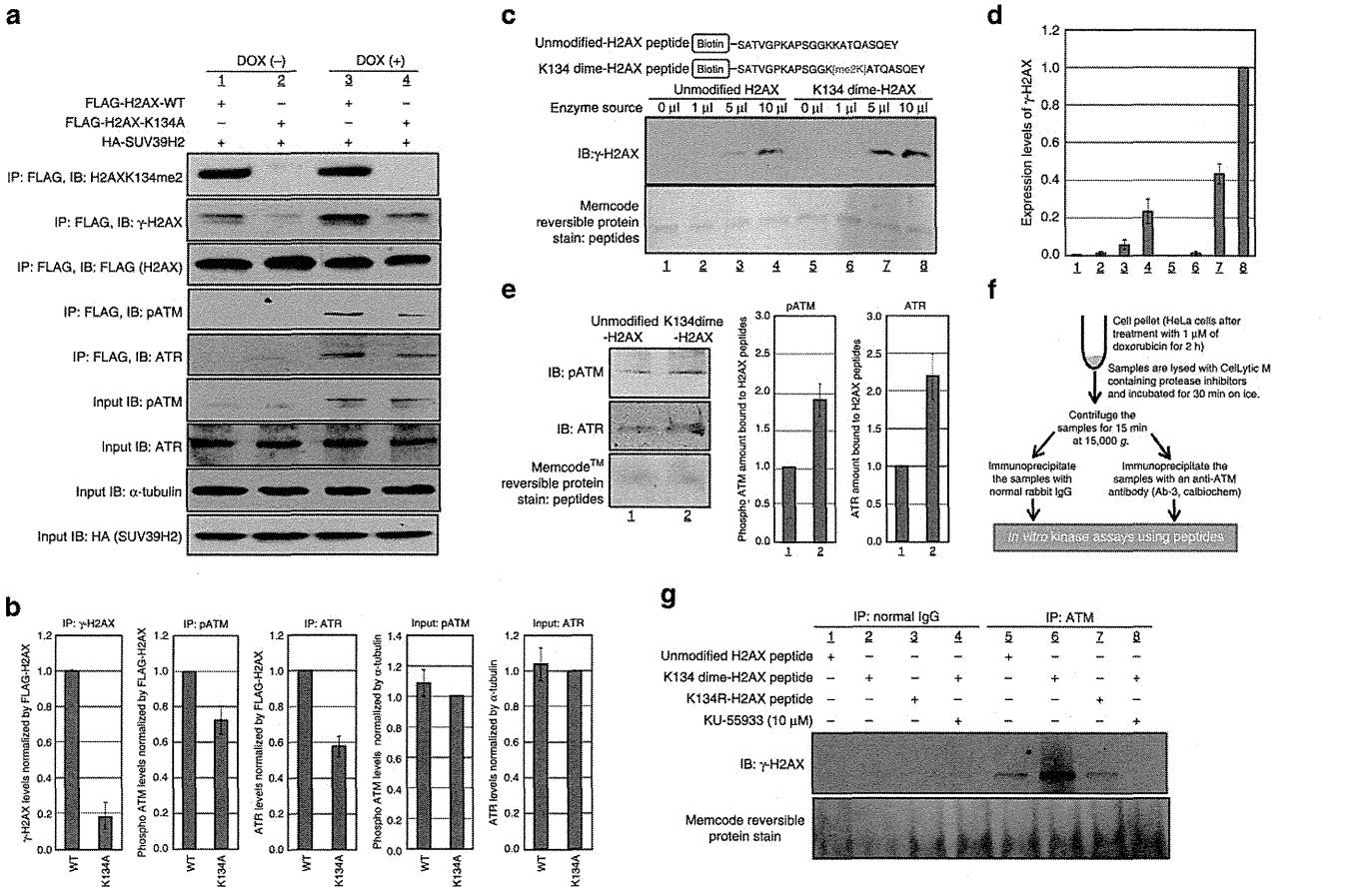

Figure 4 | H2AXK134 methylation by SUV39H2 plays an important role in γ-H2AX production. (**a**) FLAG-H2AX-WT or a FLAG-H2AX-K134A were co-expressed with HA-SUV39H2 and treated with 1 μM of doxorubicin 48 h post transfection. The samples were immunoblotted with anti-H2AXK134me2, anti-γ-H2AX, anti-FLAG, anti-phospho ATM and ATR antibodies after immunoprecipitating with anti-FLAG M2 agarose. Input protein levels of phospho-ATM, ATR, α-Tubulin and HA are also shown. (**b**) Quantification of WB results shown in **a**. γ-H2AX, phospho ATM and ATR levels after doxorubicin treatment normalized by FLAG or α-Tubulin expression levels and averaged. Results are the mean ± s.d. ($n=3$). (**c**) *In vitro* kinase and pull-down assay. Biotin-tagged unmodified H2AX peptides or biotin-tagged K134 dimethylated H2AX peptides were mixed with enzyme source (whole-cell lysates of HeLa cells). Peptides were precipitated and immunoblotted with an anti-γ-H2AX antibody. (**d**) The intensity of γ-H2AX signal was normalized by peptide amount and averaged. Results are the means ± s.d. ($n=3$). (**e**) Comparison of ATR and phospho-ATM amounts bound to unmodified-H2AX peptides and K134-dimethylated H2AX peptides. Biotin-tagged peptides were mixed with 5 μl of enzyme source (whole-cell lysates of HeLa cells). Peptides were precipitated and immunoblotted with anti-ATR and anti-phospho-ATM antibodies. Results are the means ± s.d. ($n=3$). (**f**) The schematic drawing of strategy for *in vitro* kinase assays. (**g**) Biotin-tagged unmodified H2AX peptides, biotin-tagged K134-dimethylated H2AX peptides and biotin-tagged K134R H2AX peptides were mixed with enzyme source (immunoprecipitated ATM) in the presence or absence of KU-55933. The samples were immunoblotted with an anti-γ-H2AX antibody.

K134-dimethylated peptide. These results further support our hypothesis that dimethylated K134 is critical for H2AX S139 phosphorylation.

We next examined the effect of H2AX K134 methylation on the localization of the tumour suppressor p53-binding protein 1 (TP53BP1)—one of the important mediators within the DSB repair machinery—following treatment with doxorubicin. As previously observed[1,6], TP53BP1 formed foci that co-localized with γ-H2AX in the WT MEFs; however, it was widely distributed in the *Suv39h2*$^{-/-}$ MEFs (Fig. 5a). Similarly, TP53BP1 localization was lost in RERF-LC-AI cells when SUV39H2 was knocked down (Fig. 5b).

Correlation of H2AX K134 methylation and γ-H2AX in cancer. To examine the relation between H2AX K134 methylation and γ-H2AX levels in clinical tissues, we conducted immunohistochemical analysis using tissue microarray comprising 154 cases of lung cancer. As shown in Fig. 5c, the signal intensity of both H2AX K134 methylation and γ-H2AX was notably higher in lung cancer tissues compared with normal tissues. We calculated the Spearman's correlation coefficient by ranks with ties, to clarify the statistical correlation between the two histone H2AX modifications. The Spearman's ρ-value of 0.823 ($P<0.0001$; Fig. 5d and Supplementary Table 2) supports a direct correlation between H2AX K134 methylation and γ-H2AX levels. This result was also confirmed in clinical bladder tissues (Fig. 5e,f and Supplementary Table 3).

H2AX K134 methylation regulates chemo- and radio-sensitivity. To further evaluate the effect of H2AX K134 methylation on γ-H2AX production and DNA repair, we established a dominant-negative experimental system. HeLa cells were transfected with either FLAG-H2AX-WT or FLAG-H2AX-K134A, with or without co-expression of HA-SUV39H2. After 48 h, cells were treated with 1 μM Doxorubicin for 2 h and harvested for WB analysis (Fig. 6a). SUV39H2 overexpression clearly enhanced both H2AX K134 dimethylation and S139 phosphorylation on the H2AX-WT proteins, but not the in

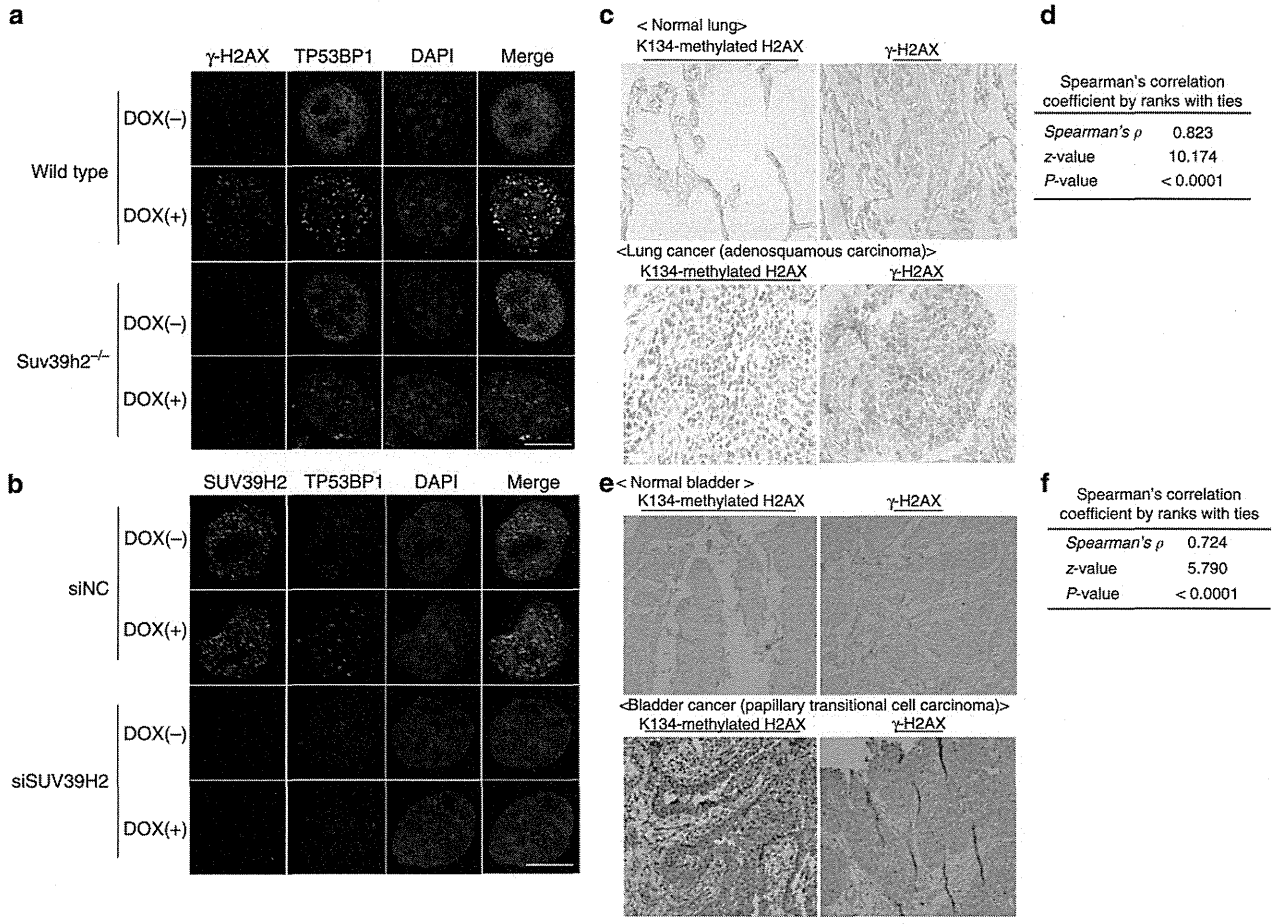

Figure 5 | H2AXK134 methylation and γ-H2AX levels are correlated in clinical tissues. (**a**) Immunocytochemical analysis of MEF-WT and MEF-Suv39h2$^{-/-}$. Cells were treated with 1 μM of doxorubicin for 1 h and stained with an anti-γ-H2AX antibody (red), an anti-TP53BP1 antibody (green) and 4′,6-diamidino-2-phenylindole dihydrochloride (DAPI; blue). Scale bar, 10 μm. (**b**) Immunocytochemical analysis of RERF-LC-AI cells after knockdown of SUV39H2. Cells were transfected with siNC and siSUV39H2. After 48 h, siRNA-transfected cells were treated with 1 μM of doxorubicin for 1 h and stained with an anti-SUV39H2 antibody (red), an anti-TP53BP1 antibody (green) and DAPI (blue). Scale bar, 10 μm. (**c**) Immunohistochemical stainings of K134-methylated H2AX and γ-H2AX in clinical lung tissues. Typically stained normal and tumour tissues are shown. Detailed clinical information and data are described in Supplementary Table 2. (**d**) Correlation of staining between K134-methylated H2AX and γ-H2AX was statistically calculated using Spearman's correlation coefficient by ranks with ties. (**e**) H2AXK134 methylation and γ-H2AX were co-expressed in clinical bladder tissues. Immunohistochemical stainings of K134-methylated H2AX and γ-H2AX in clinical bladder tissues. Typically stained normal and tumour tissues are shown. Detailed clinical information and data are described in Supplementary Table 3. (**f**) Correlation of staining between K134-methylated H2AX and γ-H2AX in clinical bladder tissues was statistically calculated using Spearman's correlation coefficient by ranks with ties.

K134-substituted proteins (Fig. 6a). We repeated the WB analysis (Supplementary Fig. 8) and quantified levels of H2AX K134 dimethylation and γ-H2AX (Fig. 6b), which showed a strong correlation between the histone H2AX K134 methylation and γ-H2AX. To examine whether exogenous H2AX proteins are appropriately incorporated into chromatin, HeLa cells transfected with FLAG-H2AX-WT or FLAG-H2AX-K134 were stained with anti-FLAG antibody after synchronizing the cells (Fig. 6c). The FLAG-tagged H2AX-WT and H2AX-K134A proteins that overlapped the strong 4′,6-diamidino-2-phenylindole stainings were detected in the heterochromatin regions in the nucleus[23,24]. In mitotic cells, we found co-localization of the exogenous H2AX proteins with condensed chromosomes, further indicating that the exogenous H2AX-WT and H2AX-K134A proteins were appropriately incorporated into the chromatin. We also confirmed the incorporation of exogenous H2AX-WT and H2AX-K134A into chromatin by WB after chromatin fractionation (Supplementary Fig. 9).

Using this dominant-negative system, we also examined the effect of K134 methylation on radio- and chemosensitivity. H2AX-K134A-overexpressing HeLa cells exhibited significantly lower viability than H2AX-WT-overexpressing HeLa cells following radiation treatment (Fig. 7a,b). Sensitivity was also shown to be dose dependent by colony-formation assay (Fig. 7c and Supplementary Fig. 10). We examined the cell cycle status in the two cell lines without radiation and found no difference (Fig. 7d,e). With regard to the effect of H2AX K134 methylation on chemosensitivity, IC50s of both cisplatin and doxorubicin treatment were significantly lower in the H2AX-K134A-overexpressed HeLa cells (cisplatin: WT = 4.82 μM, K134A = 1.26 μM; doxorubicin: WT = 4.82 μM, K134A = 1.26 μM; Fig. 7f). In summary, attenuation of H2AX K134 methylation appears to enhance both radio- and chemosensitivity of cancer cells.

Discussion

In the present study, we showed that the histone methyltransferase SUV39H2 methylates histone H2AX on lysine 134, and that this is critical for the production of γ-H2AX in cancer cells (Supplementary Fig. 11). Our binding assays revealed that the

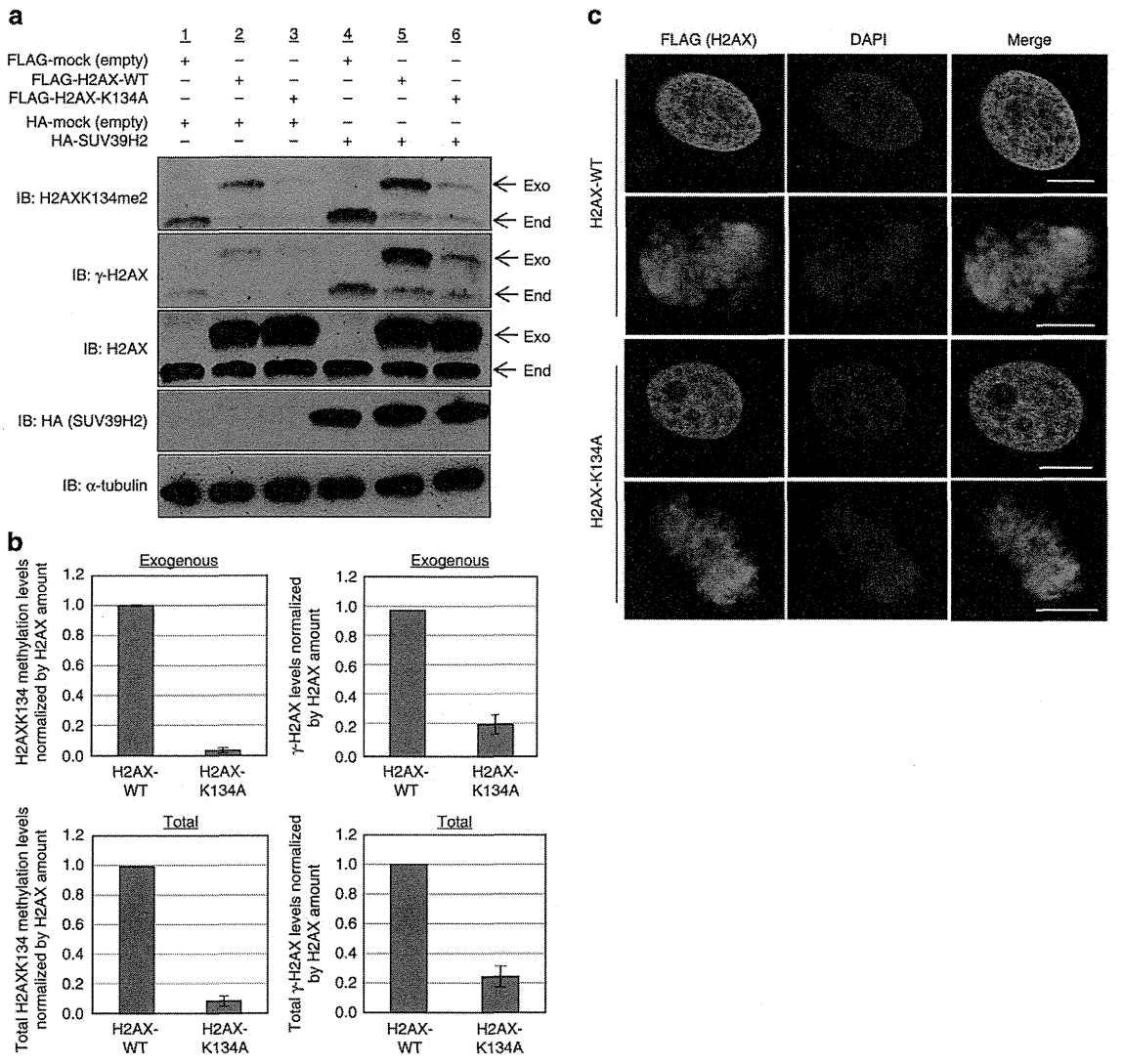

Figure 6 | Establishment of the dominant-negative system using HeLa cells transfected with FLAG-H2AX-WT and FLAG-H2AX-K134A. (**a**) HeLa cells were transfected with a FLAG-H2AX-WT, FLAG-H2AX-K134A or FLAG with HA-SUV39H2 or an HA-control. After 48 h, cells were treated with 1 μM of doxorubicin for 1 h and samples immunoblotted with anti-H2K134me2, anti-γ-H2AX, anti-H2AX, anti-HA (SUV39H2) and anti-α-Tubulin antibodies. (**b**) Quantification of exogenous and endogenous K134-dimethylated or γ-H2AX amount. The intensity of K134-dimethylated H2AX and γ-H2AX levels was normalized against H2AX. Results are the mean ± s.d. ($n = 3$). Total amount shows the sum of endogenous and exogenous expression levels. Results are the mean ± s.d. ($n = 3$). (**c**) HeLa cells were transfected with FLAG-H2AX-WT or FLAG-H2AX-K134A, and treated with 7.5 (μg ml^{-1}) of aphidicolin to synchronize the cell cycle 48 h after transfection. Next, the cells were stained with an anti-FLAG antibody (green) and 4′,6-diamidino-2-phenylindole dihydrochloride (DAPI; blue) 13 h after release from G_1 arrest. Scale bars, 10 μm.

lack of methylation at K134 reduces the affinity between the kinases responsible for γ-H2AX production and H2AX (Fig. 4b,e).

SUV39H2 can also methylate histone H3 lysine 9 and this methylation is considered to be important for organizing heterochromatin[20]. Given that chromatin structure is likely to be important for DNA repair processes, the dynamics of relevant histone modifications during this step may play important roles in organizing the process appropriately. Indeed, histone H3 K9 methylation was also reported to be a regulator of the DNA repair pathway[25,26], indicating that SUV39H2 might regulate this pathway through the methylation of both histone H2AX K134 and H3 K9. Further functional analyses may clarify the dynamics of histone modifications, the involvements of other proteins and their mutual relations in the DDR following induction of DSBs in cancer cells.

It has previously been reported that constitutive endogenous γ-H2AX foci are rare in normal primary human cells and tissues[27]. However, cancer cells and tissues show different degrees of constitutive γ-H2AX activity in the absence of exogenously induced DSBs[27,28]. Moreover, γ-H2AX is also a prognostic marker for several types of human cancer, and increased γ-H2AX levels are significantly associated with poorer prognosis of triple-negative breast cancer, endometrial cancer and NSCLC[28–31]. These results imply that high γ-H2AX expression levels may be involved in a more aggressive, highly proliferating tumour phenotype and resistance to anti-cancer treatment[30]. Given that SUV39H2 is significantly upregulated in various types of tumour tissues (Supplementary Table 1), it is possible that constitutive SUV39H2 overexpression in cancer cells may cause aberrant γ-H2AX expression, and that cancer cells might acquire more malignant phenotype, including chemo- and/or radioresistance.

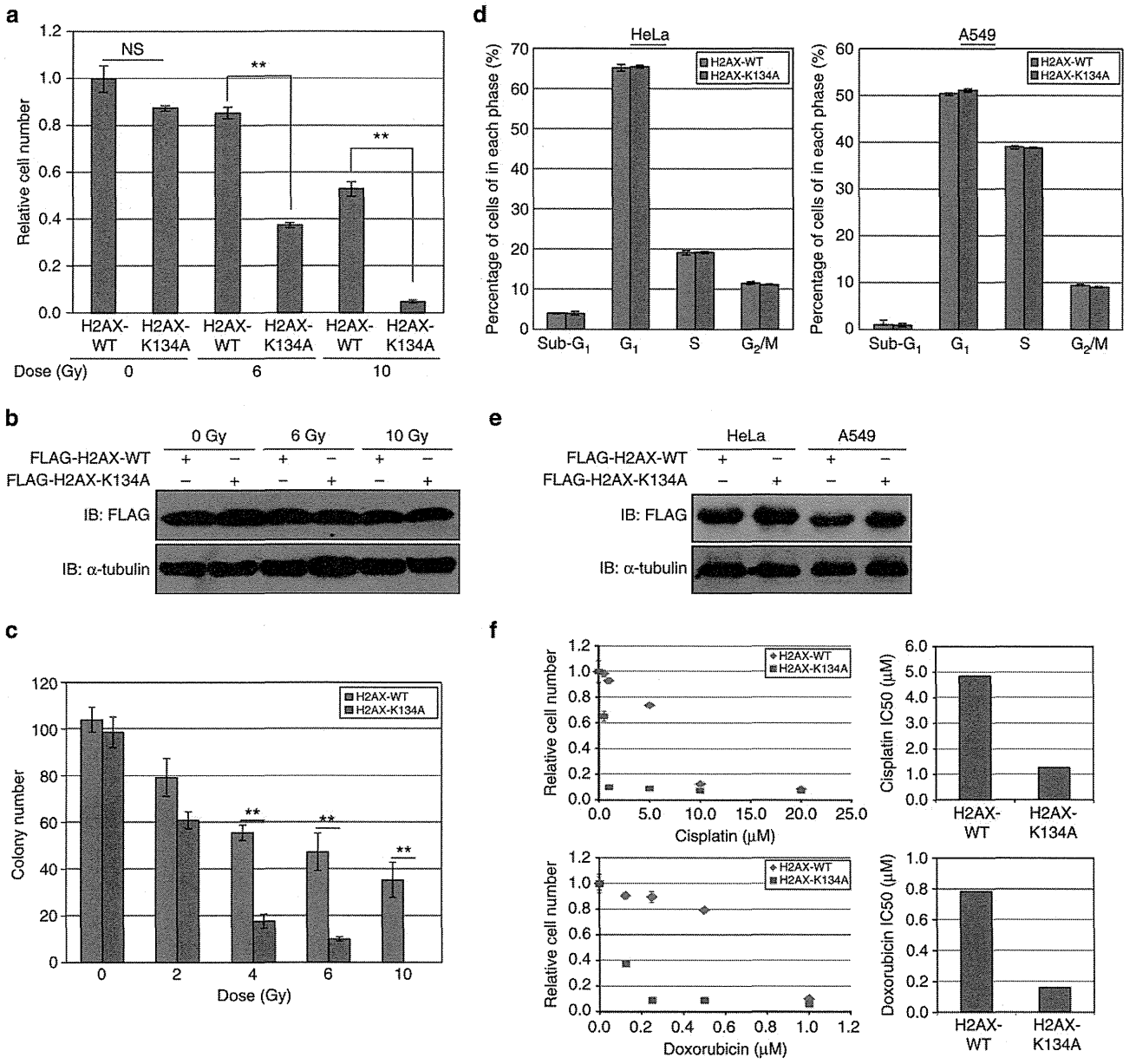

Figure 7 | SUV39H2-dependent H2AXK134 methylation regulates radiosensitivity and chemosensitivity of cancer cells. (**a**) HeLa cells were transfected with a FLAG-H2AX-WT or a FLAG-H2AX-K134A expression vector and HA-SUV39H2, then irradiated with 6 or 10 Gy of ionizing radiation 24 and 72 h post transfection. Cell viability was measured 24 h after the second irradiation. Results are the mean ± s.d. ($n=3$). *P*-values were calculated using Student's *t*-test (**$P<0.01$). n.s., not significant. (**b**) Expression of FLAG-H2AX-WT and FLAG-H2AX-K134A in HeLa cells from **a**. Samples were immunoblotted with anti-FLAG and anti-α-Tubulin antibodies. (**c**) Clonogenicity assays of HeLa cells transfected with H2AX-WT and H2AX-K134A. Cells were irradiated with 0, 2, 4, 6 and 10 Gy of ionizing radiation 24 h post transfection. Subsequently, the cells were cultured in EMEM with 0.8 mg ml^{-1} of Geneticin/G-418 for 15 days. Results are the means ± s.d. ($n=3$). *P*-values = Student's *t*-test (**$P<0.01$). (**d**) Detailed cell cycle kinetics in HeLa cells 48 h after transfection with FLAG-H2AX and FLAG-K134A. (**e**) Expression of FLAG-H2AX-WT and FLAG-H2AX-K134A in HeLa and A549 cells from **d**. (**f**) HeLa cells overexpressing FLAG-H2AX-WT or FLAG-H2AX-K134A with HA-SUV39H2 were treated with cisplatin or doxorubicin 24 h post transfection. Cell viability was measured 48 h after the drug treatment.

Importantly, γ-H2AX is considered to be a drug target[32–38] and peptide inhibitors of γ-H2AX have already been reported as potential chemotherapeutic agents[35,39]. Inhibition of γ-H2AX through interference with upstream kinase activities using caffeine, wortmannin and LY294002 resulted in significantly increased tumour cell radiosensitivity[40]. In addition, VE-821, a novel specific inhibitor of ATR[41], increased sensitivity of cancer cells to radiation and/or chemotherapy[42–45]. These findings suggest that regulation of γ-H2AX production through the inhibition of SUV39H2-depedent H2AX K134 methylation could be an attractive target for drug development. Indeed, as the expression level of SUV39H2 in normal tissues is low (Fig. 1d, and Supplementary Figs 12 and 13), this molecule could represent an ideal target for cancer therapy. Moreover, our knockdown experiments using Cell Counting kit-8 (CCK-8), Giemsa and fluorescence-activated cell sorting and clonogenicity assays revealed that SUV39H2 appears to possess oncogenic activity (Supplementary Fig. 14). According to our expression profile analysis, SUV39H1 is also overexpressed in some cancers. Moreover, knockdown of SUV39H2 significantly diminished

the γ-H2AX production even though SUV39H1 expression levels were not changed (Fig. 3a), suggesting that SUV39H2 is a critical factor that regulates γ-H2AX production. Taking these findings into account, we propose a SUV39H2 inhibitor could be used alone or in combination with DNA-damaging agents or radiotherapy in cancer patients with aberrant SUV39H2 expression.

Methods

Cell culture and clinical tissues. NCI-H1781, A549, SK-MES-1, NCI-H2170, NCI-H520, DMS 114, 293T, HeLa, SW780 and COS-7 cells were from the American Type Culture Collection in 2001 and 2003, and were tested and authenticated by DNA profiling for polymorphic short tandem-repeat markers (Supplementary Table 4). SBC-3, SBC-5 and RERF-LC-AI cells were from the Japanese Collection of Research Bioresources in 2001 and were tested and authenticated by DNA profiling for polymorphic short tandem-repeat markers (Supplementary Table 4). ACC-LC-319 cells were from the Aichi Cancer Center in 2003, and were tested and authenticated by DNA profiling for single-nucleotide polymorphism, mutation and deletion analysis (Supplementary Table 4). The SW780 line was established in 1974 by A. Leibovitz from a grade I transitional cell carcinoma.

All cell lines were grown in monolayers in appropriate media: DMEM for RERF-LC-AI, 293T and COS-7 cells; Eagle's minimum essential medium for SK-MES-1, SBC-3, SBC-5 and HeLa cells; RPMI1640 medium for NCI-H1781, ACC-LC-319, A549, NCI-H2170, NCI-H520 and DMS 114 cells; Leibovitz's L-15 for SW780 cells supplemented with 10% fetal bovine serum (FBS) and 1% antibiotic/antimycotic solution (Sigma-Aldrich). SAEC cells were maintained in small airway epithelial cell basal medium supplemented with 52 μg ml^{-1} bovine pituitary extract, 0.5 ng ml^{-1} human recombinant epidermal growth factor, 0.5 μg ml^{-1} hydrocortisone, 0.5 μg ml^{-1} epinephrine, 10 μg ml^{-1} transferrin, 5 μg ml^{-1} insulin, 0.1 ng ml^{-1} retinoic acid, 6.5 ng ml^{-1} triiodothyronine, 50 μg ml^{-1} Gentamicin/Amphotericin-B (GA-1000) and 50 μg ml^{-1} fatty acid-free BSA. All cells were maintained at 37 °C in humid air with 5% CO_2 condition, except for SW780 cells (without CO_2). Cells were transfected with FuGENE 6 or FuGENE HD (Roche Applied Science) according to manufacturer's protocols[46,47]. The use of all clinical materials in this study was approved by Ethics Committees of Institute of Medical Science at the University of Tokyo.

Antibodies. The following primary antibodies were used: anti-FLAG (rabbit, F7425; Sigma-Aldrich; dilution used in WB: 1:3,000, ICC: 1:500), anti-FLAG (mouse, M2; Sigma-Aldrich; dilution used in ICC: 1:500), anti-HA (Y-11; Santa Cruz Biotechnology; dilution used in WB: 1:500), anti-SUV39H1 (#8729; Cell Signaling Technology; dilution used in WB: 1:500), anti-H2AX (07-627; Millipore; dilution used in WB: 1:500, IP: 1:250), anti-γ-H2AX (05-636; Millipore; dilution used in WB: 1:500, ICC: 1:250, immunohistochemistry: 1:250), anti-ATM (ab2629; Abcam; dilution used in WB: 1:500), anti-phospho-ATM (ab81292; Abcam; dilution used in WB: 1:500), anti-ATR (#2790; Cell Signaling Technology; dilution used in WB: 1:500), anti-phospho-Chk2 (#2661; Cell Signaling Technology; dilution used in WB: 1:500), anti-α-Tubulin (T6199; Sigma-Aldrich; dilution used in WB: 1:500), anti-TP53BP1 (Clone BP13; Millipore; dilution used in ICC: 1:250) for RERF-LC-AI cells, anti-TP53BP1 (#4937; Cell Signaling Technology; dilution used in ICC: 1:250) for mouse MEF cells, anti-H2A (ab13923; Abcam; dilution used in WB: 1:1,000), anti-histone H3 (ab1791; Abcam; dilution used in WB: 1:1,000), anti-histone H4 (#2592S; Cell Signaling Technology; dilution used in WB: 1:1,000), anti-ATM (Ab-3; Calbiochem; dilution used in IP: 1:100) for IP and anti-ACTB (#2592S; Cell Signaling Technology; dilution used in WB: 1:1,000). An anti-SUV39H2 antibody (Sigma-Aldrich; dilution used in WB: 1:250, ICC: 1:250) and an anti-K134 di-methylated H2AX antibody (Sigma-Aldrich; dilution used in WB: 1:500, ICC: 1:250, immunohistochemistry: 1:250) were produced in rabbit immunized with a synthetic peptide.

Quantitative real-time PCR. For quantitative real-time PCR reactions, specific primers for all *GAPDH* (housekeeping gene), *SDH* (housekeeping gene) and *SUV39H2* were designed (primer sequences in Supplementary Table 5). PCR reactions were performed using the LightCycler 480 System (Roche Applied Science) and ViiA 7 real-time PCR system (Life Technologies, Carlsbad, CA), following the manufacturer's protocol. Messenger RNA levels were normalized to *GAPDH* and *SDH* expression.

***In vitro* methyltransferase assay.** For the *in vitro* methyltransferase assay, recombinant Histone H2AX (#14-576, Millipore) was incubated with recombinant SUV39H2 enzyme using 1 μCi S-adenosyl-L-[methyl-^{3}H]-methionine (SAM; PerkinElmer) as the methyl donor in a mixture of 10 μl of methylase activity buffer (50 mM Tris-HCl at pH8.8, 10 mM dithiothreitol and 10 mM $MgCl_2$), for 2 h at 30 °C[48–51]. Proteins were resolved on a 5–20 % SDS–PAGE gel (Ready Gel; Bio-Rad) and visualized by MemCode Reversible Stain (Thermo Scientific) and fluorography.

Mass spectrometry. Histone H2AX samples that reacted with SUV39H2 were separated on SDS–PAGE and stained with Simply Blue Safe Stain (Life Technologies). The excised Histone H2AX bands were reduced in 10 mM tris (2-carboxyethyl) phosphine (Sigma-Aldrich) with 50 mM ammonium bicarbonate (Sigma-Aldrich) for 30 min at 37 °C and alkylated in 50 mM iodoacetamide (Sigma-Aldrich) with 50 mM ammonium bicarbonate for 45 min in the dark at 25 °C. Trypsin GOLD (Promega) solution was added with the enzyme to protein ratio at 1/50 (w/w) and incubated at 37 °C for 16 h. The resulting peptides were extracted from gel fragments and separated on a 0.1 × 200 mm homemade C_{18} column using 45 min linear gradient from 2% to 35% acetonitrile in 0.1% formic acid, with flow rate at 200 nl min^{-1}. The eluting peptides were analysed with HCTultra ETD II mass spectrometer (Bruker Daltonics). The acquired MS and collision-induced dissociation (CID) MS/MS spectra were processed with Compass DataAnalysis 4.0 (Bruker Daltonics) and BioTools 3.1 software (Bruker Daltonics), followed by the database search on in-house Mascot server ver.2.3.01 (Matrix Science). We accepted the peptide identifications satisfying the Expectation value <0.05 in Mascot Database search.

Western blotting. Samples were prepared from the cells lysed with CelLytic M cell lysis reagent (Sigma-Aldrich) containing a complete protease inhibitor cocktail (Roche Applied Science)[51], and whole cell lysates or IP products were transferred to nitrocellulose membrane. Protein bands were detected by incubating with horseradish peroxidase (HRP)-conjugated antibodies (GE Healthcare) and visualizing with enhanced chemiluminescence (GE Healthcare). We declare that our blots were evenly exposed in each membrane and that the blots are not clopped to the bands.

Immunocytochemistry. Cultured cells were fixed in 4% paraformaldehyde in 0.1 M phosphate buffer (pH 7.4) at room temperature for 30 min, permeabilized in 0.1% Triton X-100 (Sigma-Aldrich) for 3 min on ice and blocked with 3% BSA for 1 h at room temperature[49]. Fixed cells were incubated with primary antibodies overnight at 4 °C, incubated with Alexa Fluor-conjugated secondary antibody (Molecular Probes, Life Technologies) and observed using a Leica confocal microscopy (SP5 Tandem Scanner Spectral 2-Photon Confocal).

Immunohistochemical analysis. SUV39H2 expression and status of histone H2AX K134 methylation status and S139 phosphorylation in clinical tissues were examined by immunohistochemical analysis[49,50,52–57]. EnVision + kit/HRP kit (Dako) was applied and slides of paraffin-embedded lung tumour specimens were processed under high pressure (125 °C, 30 s) in antigen-retrieval solution, high pH 9 (S2367, Dako), treated with peroxidase-blocking reagent and then treated with protein-blocking reagent (K130, X0909, Dako). Tissue sections were incubated with a rabbit anti-SUV39H2, a rabbit anti-H2AXK134me2 polyclonal antibody and a mouse anti-γ-H2AX antibody, followed by HRP-conjugated secondary antibody (Dako). Antigen was visualized with substrate chromogen (Dako liquid DAB chromogen; Dako). Finally, tissue specimens were stained with Mayer's haematoxylin (Hematoxylin QS; Vector Laboratories, Burlingame, CA, USA) for 20 s to discriminate the nucleus from the cytoplasm. The intensity of H2AXK134 methylation and H2AXS139 phosphorylation was evaluated using the following criteria: strong positive (scored as 2 +), brown staining in >50% of tumour cells completely obscuring cytoplasm; weak positive (1 +), any lesser degree of brown staining appreciable in tumour cell cytoplasm; and absent (scored as 0), no appreciable staining in tumour cells. Cases were accepted as strongly positive if two or more investigators independently defined them as such.

Fluorescence-activated cell sorting. SW780 and A549 cells were treated with siSUV39H2 or control siRNAs (siEGFP and siNC) and cultured in a CO_2 incubator at 37 °C for 72 h. Aliquots of 1 × 10^5 cells were collected by trypsinization and stained with propidium iodide following the manufacturer's instructions (Cayman Pharma, Neratovice, Czech Republic). Cells were analysed by FACScan (Beckman Coulter, Brea, CA) with MultiCycle for Windows software (Beckman Coulter) for detailed cell cycle status[58]. The percentages of cells in G_0/G_1, S and G_2/M phases of the cell cycle were determined from at least 20,000 ungated cells.

Coupled cell cycle and cell proliferation assay. A 5′-bromo-2′-deoxyuridine (BrdU) flow kit (BD Pharmingen, San Diego, CA) was used to determine the cell cycle kinetics and to measure the incorporation of BrdU into DNA of proliferating cells[48,54,59–61]. The assay was performed according to the manufacturer's protocol. Briefly, cells were cultured in the presence of 10 μM of BrdU for 30 min at 37 °C. Next, both floating and adherent cells were pooled from triplicate wells per treatment point, fixed in a solution containing paraformaldehyde and the detergent saponin, and incubated for 1 h with DNase at 37 °C (30 μg per sample). Fluorescein isothiocyanate-conjugated anti-BrdU antibody (1:50 dilution in Wash buffer; BD Pharmingen) was added and incubation continued for 20 min at room temperature. Cells were washed in Wash buffer and total DNA was stained with 7-amino-actinomycin D (20 μl per sample), followed by flow cytometric analysis using FACScan (Beckman Coulter) and total DNA content (7-amino-actinomycin D) was determined by using CXP Analysis Software Ver. 2.2 (Beckman Coulter).

Immunoprecipitation. Transfected 293T cells or HeLa cells were lysed with CelLytic M cell lysis reagent (Sigma-Aldrich) containing a complete protease inhibitor cocktail (Roche Applied Science). In a typical IP reaction, 300 μg of whole-cell extract was incubated with an optimum concentration of primary antibody. After the beads had been washed three times in 1 ml of TBS buffer (pH 7.6), proteins that bound to the beads were eluted by boiling in Lane Marker Reducing Sample Buffer (Thermo Scientific).

siRNA transfection. siRNA oligonucleotide duplexes were purchased from Sigma-Aldrich for targeting the human *SUV39H2* transcript. siNC was used as a control siRNA. The siRNA sequences are described in Supplementary Table 6. siRNA duplexes (100 nM final concentration) were transfected into bladder and lung cancer cell lines with Lipofectamine 2000 (Life Technologies)[62–64].

Mouse embryonic fibroblast. Mouse *Suv39h2* WT and *Suv39h2*$^{-/-}$ MEF cells were established by Dr Thomas Jenuwein group[22]. Cells were cultured with DMEM supplemented with 10% FBS, 1% antibiotic/antimycotic solution (Sigma-Aldrich), 2 mM L-glutamine, 0.1 mM β-mercaptoethanol, 1 × non-essential amino acid solution (Life Technologies) and sodium pyruvate. Phenotype of MEF cells were confirmed by CCK-8 (Dojindo) and coupled cell cycle and cell proliferation assay. Mouse H2AX$^{-/-}$ MEF cells were established by Dr Andre Nussenzweig group[9] and cells were cultured with DMEM supplemented with 10% FBS and 1% antibiotic/antimycotic solution (Sigma-Aldrich). We confirmed that exogenous FLAG-tagged H2AX-WT and H2AX-K134A proteins were appropriately incorporated into chromatin (Supplementary Fig. 6).

***In vitro* kinase and pull-down assay.** HeLa cells were lysed with CelLytic M cell lysis reagent (Sigma-Aldrich) containing protease and phosphatase inhibitors 2 h after treatment with 1 μM of doxorubicin and used as enzyme source. Biotin-tagged unmethylated H2AX peptide (Biotin-SATVGPKAPSGGKKATQASQEY) or biotin-tagged methylated H2AX peptide (Biotin-SATVGPKAPSGGK[me2K] ATQASQEY) is mixed with different amount of doxorubicin-induced HeLa cell lysates in the kinase buffer (50 mM HEPES, pH 7.5, 50 mM potassium chloride, 5 mM magnesium chloride, 10% glycerol, 1 mM ATP and 1 mM dithiothreitol) for 90 min at 30 °C. Peptides were precipitated with Dynabeads M-280 streptavidin (Life Technologies) and the samples were separated on SDS–PAGE using the Tris-Tricine Precast Gel (456-3063, Bio-Rad). Subsequently, WB was performed using an anti-γ-H2AX antibody (Millipore). The nitrocellulose membrane for the WB was stained with MemCode Reversible Stain (Thermo Scientific) to quantify the amount of peptides.

Dominant-negative experiments. HeLa cells were cultured for 24 h and transfected with a FLAG-H2AX-WT expression vector, a FLAG-H2AX-K134A expression vector or a FLAG-Mock (Empty) vector and an HA-SUV39H2 expression vector using FuGENE HD transfection reagent (Roche Applied Science). Cells were harvested 48 h after transfection and lysed with CelLytic M cell lysis reagent (Sigma-Aldrich) containing a complete protease inhibitor cocktail (Roche Applied Science). Samples were separated by standard SDS–PAGE and subsequently immunoblotted with anti-H2AK134me2, anti-γ-H2AX antibody, anti-H2AX, anti-FLAG and anti-α-Tubulin antibodies. Endogenous or exogenous H2AX K134 methylation and γ-H2AX levels were quantified by GS-800 calibrated imaging densitometer (Bio-Rad).

Radiosensitivity and chemosensitivity experiments. With regard to the knockdown experiment, we cultured RERF-LC-AI cells for 24 h and transfected control siRNA (siNC) and two independent SUV39H2 siRNAs into the cells. After 48 h, the cells were irradiated with 3 or 6 Gy of ionizing radiation by cabinet X-ray system (Newco), and cell viability was measured by CCK-8 (Dojindo) 24 h after irradiation. In addition, RERF-LC-AI cells were treated with various concentrations of cisplatin or doxorubicin 48 h after treatment with siRNAs, and the cells were cultured for additional 48 h. Subsequently, cell viability was measured by CCK-8 and the SigmaPlot software (Systat Software) was used to calculate IC50. As for the dominant-negative experiment, HeLa cells were transfected with a FLAG-H2AX-WT or a FLAG-H2AX-K134A expression vector with an HA-SUV39H2 expression vector using FuGENE HD (Roche Applied Science) reagent. After 24 and 72 h, transfected HeLa cells were irradiated with 6 or 10 Gy of ionizing radiation by cabinet X-ray system (Newco) and cell viability was measured by CCK-8 (Dojindo) 24 h after the second irradiation. In addition, vector-transfected HeLa cells were treated with various concentrations of cisplatin or doxorubicin 24 h after the transfection, and the cells were cultured for additional 48 h. Next, cell viability was measured by CCK-8. IC50 was calculated with the SigmaPlot software.

Colony formation assays. HeLa cells, cultured in EMEM with 10% FBS, were transfected with a p3xFLAG-H2AX-WT vector or a p3xFLAG-H2AX-K134A mutant vector, and an HA-SUV39H2 vector using FuGENE HD. Cells were irradiated with 0, 2, 4, 6 and 10 Gy of ionizing radiation by cabinet X-ray system 24 h after the transfection. Subsequently, the cells were cultures in the medium containing 0.8 mg ml^{-1} of Geneticin/G-418 for 15 days. The colony number was calculated by GS-800-calibrated densitometer and results are the means ± s.d. of three independent experiments. *P*-values were calculated using Student's *t*-test.

Statistical analysis. Each experiment has been repeated at least three times. Values were presented as the mean plus or minus s.d. Statistical analyses were performed using unpaired Student's *t*-test (two groups) and Kruskal–Wallis one-way analysis of variance (more than two groups). Significant difference between groups was noted when *P*-value was <0.05.

References

1. Moore, J. D. & Krebs, J. E. Histone modifications and DNA double-strand break repair. *Biochem. Cell Biol.* **82,** 446–452 (2004).
2. Lowndes, N. F. & Toh, G. W. DNA repair: the importance of phosphorylating histone H2AX. *Curr. Biol.* **15,** R99–R102 (2005).
3. Pinto, D. M. & Flaus, A. Structure and function of histone H2AX. *Subcell. Biochem.* **50,** 55–78 (2010).
4. Bartova, E., Krejci, J., Harnicarova, A., Galiova, G. & Kozubek, S. Histone modifications and nuclear architecture: a review. *J. Histochem. Biochem.* **56,** 711–721 (2008).
5. Bonner, W. M. *et al.* GammaH2AX and cancer. *Nat. Rev. Cancer* **8,** 957–967 (2008).
6. Rogakou, E. P., Pilch, D. R., Orr, A. H., Ivanova, V. S. & Bonner, W. M. DNA double-stranded breaks induce histone H2AX phosphorylation on serine 139. *J. Biol. Chem.* **273,** 5858–5868 (1998).
7. Harper, J. W. & Elledge, S. J. The DNA damage response: ten years after. *Mol. Cell* **28,** 739–745 (2007).
8. Celeste, A. *et al.* Histone H2AX phosphorylation is dispensable for the initial recognition of DNA breaks. *Nat. Cell Biol.* **5,** 675–679 (2003).
9. Celeste, A. *et al.* Genomic instability in mice lacking histone H2AX. *Science* **296,** 922–927 (2002).
10. Messick, T. E. & Greenberg, R. A. The ubiquitin landscape at DNA double-strand breaks. *J. Cell Biol.* **187,** 319–326 (2009).
11. Stewart, G. S. *et al.* The RIDDLE syndrome protein mediates a ubiquitin-dependent signaling cascade at sites of DNA damage. *Cell* **136,** 420–434 (2009).
12. Mailand, N. *et al.* RNF8 ubiquitylates histones at DNA double-strand breaks and promotes assembly of repair proteins. *Cell* **131,** 887–900 (2007).
13. Doil, C. *et al.* RNF168 binds and amplifies ubiquitin conjugates on damaged chromosomes to allow accumulation of repair proteins. *Cell* **136,** 435–446 (2009).
14. Pan, M. R., Peng, G., Hung, W. C. & Lin, S. Y. Monoubiquitination of H2AX protein regulates DNA damage response signaling. *J. Biol. Chem.* **286,** 28599–28607 (2011).
15. Bassing, C. H. *et al.* Increased ionizing radiation sensitivity and genomic instability in the absence of histone H2AX. *Proc. Natl Acad. Sci. USA* **99,** 8173–8178 (2002).
16. Fernandez-Capetillo, O., Lee, A., Nussenzweig, M. & Nussenzweig, A. H2AX: the histone guardian of the genome. *DNA Repair* **3,** 959–967 (2004).
17. McKinnon, P. J. & Caldecott, K. W. DNA strand break repair and human genetic disease. *Annu. Rev. Genomics Hum. Genet.* **8,** 37–55 (2007).
18. Jeggo, P. A. & Lobrich, M. DNA double-strand breaks: their cellular and clinical impact? *Oncogene* **26,** 7717–7719 (2007).
19. Allis, C. D. *et al.* New nomenclature for chromatin-modifying enzymes. *Cell* **131,** 633–636 (2007).
20. O'Carroll, D. *et al.* Isolation and characterization of Suv39h2, a second histone H3 methyltransferase gene that displays testis-specific expression. *Mol. Cell Biol.* **20,** 9423–9433 (2000).
21. Garcia-Cao, M., O'Sullivan, R., Peters, A. H., Jenuwein, T. & Blasco, M. A. Epigenetic regulation of telomere length in mammalian cells by the Suv39h1 and Suv39h2 histone methyltransferases. *Nat. Genet.* **36,** 94–99 (2004).
22. Peters, A. H. *et al.* Loss of the Suv39h histone methyltransferases impairs mammalian heterochromatin and genome stability. *Cell* **107,** 323–337 (2001).
23. Daury, L. & Trouche, D. Analysis of histone deposition on specific DNA elements in living mammalian cells. *BioTechniques* **35,** 326–332 (2003).
24. Gertych, A., Oh, J. H., Wawrowsky, K. A., Weisenberger, D. J. & Tajbakhsh, J. 3-D DNA methylation phenotypes correlate with cytotoxicity levels in prostate and liver cancer cell models. *BMC Pharmacol. Toxicol.* **14,** 11 (2013).
25. Ayrapetov, M. K., Gursoy-Yuzugullu, O., Xu, C., Xu, Y. & Price, B. D. DNA double-strand breaks promote methylation of histone H3 on lysine 9 and transient formation of repressive chromatin. *Proc. Natl Acad. Sci. USA* **111,** 9169–9174 (2014).
26. Sun, Y. *et al.* Histone H3 methylation links DNA damage detection to activation of the tumour suppressor Tip60. *Nat. Cell Biol.* **11,** 1376–1382 (2009).
27. Sedelnikova, O. A. & Bonner, W. M. GammaH2AX in cancer cells: a potential biomarker for cancer diagnostics, prediction and recurrence. *Cell Cycle* **5,** 2909–2913 (2006).

28. Nagelkerke, A. *et al.* Constitutive expression of gamma-H2AX has prognostic relevance in triple negative breast cancer. *Radiother. Oncol.* **101,** 39–45 (2011).
29. Brunner, A. H. *et al.* Expression of gamma-H2AX in endometrial carcinomas: an immunohistochemical study with p53. *Gynecol. Oncol.* **121,** 206–211 (2011).
30. Matthaios, D. *et al.* gamma-H2AX expression detected by immunohistochemistry correlates with prognosis in early operable non-small cell lung cancer. *OncoTargets Ther.* **5,** 309–314 (2012).
31. Jackson, J. P., Lindroth, A. M., Cao, X. & Jacobsen, S. E. Control of CpNpG DNA methylation by the KRYPTONITE histone H3 methyltransferase. *Nature* **416,** 556–560 (2002).
32. Dickey, J. S. *et al.* H2AX: functional roles and potential applications. *Chromosoma* **118,** 683–692 (2009).
33. Helleday, T., Petermann, E., Lundin, C., Hodgson, B. & Sharma, R. A. DNA repair pathways as targets for cancer therapy. *Nat. Rev. Cancer* **8,** 193–204 (2008).
34. Hickson, I. *et al.* Identification and characterization of a novel and specific inhibitor of the ataxia-telangiectasia mutated kinase ATM. *Cancer Res.* **64,** 9152–9159 (2004).
35. Kao, J. *et al.* gamma-H2AX as a therapeutic target for improving the efficacy of radiation therapy. *Curr. Cancer Drug Targets* **6,** 197–205 (2006).
36. Redon, C. E. *et al.* Histone gammaH2AX and poly(ADP-ribose) as clinical pharmacodynamic biomarkers. *Clin. Cancer Res.* **16,** 4532–4542 (2010).
37. Veuger, S. J., Curtin, N. J., Richardson, C. J., Smith, G. C. & Durkacz, B. W. Radiosensitization and DNA repair inhibition by the combined use of novel inhibitors of DNA-dependent protein kinase and poly(ADP-ribose) polymerase-1. *Cancer Res.* **63,** 6008–6015 (2003).
38. Wang, D. & Lippard, S. J. Cellular processing of platinum anticancer drugs. *Nat. Rev. Drug Discov.* **4,** 307–320 (2005).
39. Taneja, N. *et al.* Histone H2AX phosphorylation as a predictor of radiosensitivity and target for radiotherapy. *J. Biol. Chem.* **279,** 2273–2280 (2004).
40. Kao, J., Lavaf, A., Lan, C. & Fu, S. Inhibition of gamma-H2AX after ionizing radiation as a biological surrogate of impaired upstream DNA damage signaling and radiosensitivity. *J. Cancer Mol.* **5,** 49–54 (2010).
41. Reaper, P. M. *et al.* Selective killing of ATM- or p53-deficient cancer cells through inhibition of ATR. *Nat. Chem. Biol.* **7,** 428–430 (2011).
42. Chaudhuri, L. *et al.* CHK1 and WEE1 inhibition combine synergistically to enhance therapeutic efficacy in acute myeloid leukemia ex vivo. *Haematologica* **99,** 688–696 (2014).
43. Huntoon, C. J. *et al.* ATR inhibition broadly sensitizes ovarian cancer cells to chemotherapy independent of BRCA status. *Cancer Res.* **73,** 3683–3691 (2013).
44. Prevo, R. *et al.* The novel ATR inhibitor VE-821 increases sensitivity of pancreatic cancer cells to radiation and chemotherapy. *Cancer Biol. Ther.* **13,** 1072–1081 (2012).
45. Vavrova, J. *et al.* Inhibition of ATR kinase with the selective inhibitor VE-821 results in radiosensitization of cells of promyelocytic leukaemia (HL-60). *Radiat. Environ. Biophys.* **52,** 471–479 (2013).
46. Hamamoto, R. *et al.* SMYD3 encodes a histone methyltransferase involved in the proliferation of cancer cells. *Nat. Cell Biol.* **6,** 731–740 (2004).
47. Hamamoto, R. *et al.* Enhanced SMYD3 expression is essential for the growth of breast cancer cells. *Cancer Sci.* **97,** 113–118 (2006).
48. Cho, H. S. *et al.* RB1 methylation by SMYD2 enhances cell cycle progression through an increase of RB1 phosphorylation. *Neoplasia* **14,** 476–486 (2012).
49. Takawa, M. *et al.* Histone lysine methyltransferase SETD8 promotes carcinogenesis by deregulating PCNA expression. *Cancer Res.* **72,** 3217–3227 (2012).
50. Cho, H. S. *et al.* Enhanced HSP70 lysine methylation promotes proliferation of cancer cells through activation of Aurora kinase B. *Nat. Commun.* **3,** 1072 (2012).
51. Cho, H. S. *et al.* Demethylation of RB regulator MYPT1 by histone demethylase LSD1 promotes cell cycle progression in cancer cells. *Cancer Res.* **71,** 1–6 (2011).
52. Takawa, M. *et al.* Validation of the histone methyltransferase EZH2 as a therapeutic target for various types of human cancer and as a prognostic marker. *Cancer Sci.* **102,** 1298–1305 (2011).
53. Kogure, M. *et al.* Deregulation of the histone demethylase JMJD2A is involved in human carcinogenesis through regulation of the G/S transition. *Cancer Lett.* **336,** 76–84 (2013).
54. Toyokawa, G. *et al.* Histone lysine methyltransferase Wolf-Hirschhorn Syndrome Candidate 1 is involved in human carcinogenesis through regulation of the Wnt Pathway. *Neoplasia* **13,** 887–898 (2011).
55. Toyokawa, G. *et al.* The histone demethylase JMJD2B plays an essential role in human carcinogenesis through positive regulation of cyclin-dependent kinase 6. *Cancer Prev. Res. (Phila.)* **4,** 2051–2061 (2011).
56. Toyokawa, G. *et al.* Minichromosome Maintenance Protein 7 is a potential therapeutic target in human cancer and a novel prognostic marker of non-small cell lung cancer. *Mol. Cancer* **10,** 65 (2011).
57. Unoki, M. *et al.* UHRF1 is a novel molecular marker for diagnosis and the prognosis of bladder cancer. *Br J Cancer* **101,** 98–105 (2009).
58. Cho, H. S. *et al.* Enhanced expression of EHMT2 is involved in the proliferation of cancer cells through negative regulation of SIAH1. *Neoplasia* **13,** 676–684 (2011).
59. Hayami, S. *et al.* Overexpression of LSD1 contributes to human carcinogenesis through chromatin regulation in various cancers. *Int. J. Cancer* **128,** 574–586 (2011).
60. Hayami, S. *et al.* Overexpression of the JmjC histone demethylase KDM5B in human carcinogenesis: involvement in the proliferation of cancer cells through the E2F/RB pathway. *Mol. Cancer* **9,** 59 (2010).
61. Cho, H. S. *et al.* The JmjC domain-containing histone demethylase KDM3A is a positive regulator of the G1/S transition in cancer cells via transcriptional regulation of the HOXA1 gene. *Int. J. Cancer* **131,** E179–E189 (2012).
62. Kang, D. *et al.* The histone methyltransferase Wolf-Hirschhorn syndrome candidate 1-like 1 (WHSC1L1) is involved in human carcinogenesis. *Genes Chromosomes Cancer* **52,** 126–139 (2013).
63. Kogure, M. *et al.* The oncogenic polycomb histone methyltransferase EZH2 methylates lysine 120 on histone H2B and competes ubiquitination. *Neoplasia* **15,** 1251–1261 (2013).
64. Yoshimatsu, M. *et al.* Dysregulation of PRMT1 and PRMT6, Type I arginine methyltransferases, is involved in various types of human cancers. *Int. J. Cancer* **128,** 562–573 (2011).

Acknowledgements

We are grateful to Drs Yataro Daigo, Vassiliki Saloura, Gottfried Von Keudell, Deng Zhenzong, Kyohei Arita, Reem Ibrahim, Hyun-Soo Cho and Gouji Toyokawa for technical support and helpful discussion, to Dr Nicholas Shukeir for providing *Suv39h2*$^{-/-}$ MEF cells and to Dr Andre Nussenzweig for providing H2AX$^{-/-}$ MEF cells. We also thank the member of Nakamura laboratory in the University of Chicago for kind support.

Author contributions

K.S., Y.N. and R.H. designed this study and performed all experiments with the help of L.P and M.N. K.U. performed the mass spectrometric analysis. T.J. provided WT and Suv39h2$^{-/-}$ MEF cells. K.S. and R.H. wrote this manuscript, and L.P., M.N., T.J. and Y.N. critically read the manuscript and gave valuable suggestions. All authors read and approved the final manuscript.

Additional information

Supplementary Information accompanies this paper at http://www.nature.com/naturecommunications

Competing financial interests: Y. Nakamura is a stock holder and a scientific advisor of Oncotherapy Science, and also has research grants from Oncotherapy Science. All other authors declare no competing financial interests.

Reprints and permission information is available online at http://npg.nature.com/reprintsandpermissions/

How to cite this article: Sone, K. *et al.* Critical role of lysine 134 methylation on histone H2AX for γ-H2AX production and DNA repair. *Nat. Commun.* 5:5691 doi: 10.1038/ncomms6691 (2014).